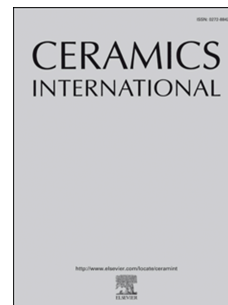


Journal Pre-proof

Design and development of Ga-substituted Z-type hexaferrites for microwave absorber applications: Mössbauer, static and dynamic properties

Preksha N. Dhruv, Robert C. Pullar, Charanjeet Singh, Francisco E. Carvalho, Rajshree B. Jotania, Sher Singh Meena, Jasbir Singh



PII: S0272-8842(20)32611-0

DOI: <https://doi.org/10.1016/j.ceramint.2020.08.231>

Reference: CERI 26333

To appear in: *Ceramics International*

Received Date: 27 April 2020

Revised Date: 12 August 2020

Accepted Date: 24 August 2020

Please cite this article as: P.N. Dhruv, R.C. Pullar, C. Singh, F.E. Carvalho, R.B. Jotania, S.S. Meena, J. Singh, Design and development of Ga-substituted Z-type hexaferrites for microwave absorber applications: Mössbauer, static and dynamic properties, *Ceramics International* (2020), doi: <https://doi.org/10.1016/j.ceramint.2020.08.231>.

This is a PDF file of an article that has undergone enhancements after acceptance, such as the addition of a cover page and metadata, and formatting for readability, but it is not yet the definitive version of record. This version will undergo additional copyediting, typesetting and review before it is published in its final form, but we are providing this version to give early visibility of the article. Please note that, during the production process, errors may be discovered which could affect the content, and all legal disclaimers that apply to the journal pertain.

© 2020 Published by Elsevier Ltd.

Design and Development of Ga-substituted Z-type Hexaferrites for Microwave Absorber Applications: Mössbauer, Static and Dynamic properties

Preksha N. Dhruv^a, Robert C. Pullar^b, Charanjeet Singh^c, Francisco E. Carvalho^{d, e}, Rajshree B. Jotania^{a*}, Sher Singh Meena^{f,**}, Jasbir Singh^g

^aDepartment of Physics, University School of Sciences, Gujarat University, Ahmedabad 380 009, India

^bDepartment of Engineering of Materials and Ceramics/CICECO - Aveiro Institute of Materials, University of Aveiro, Aveiro 3810-193, Portugal

^cDepartment of Electronics and Communication Engineering, Lovely Professional University, Phagwara, Punjab 144411, India

^dInstituto Tecnológico de Aeronáutica, Praça Mal. Eduardo Gomes, 50, São José dos Campos 12.228-900, Brazil

^eInstituto de Estudos Avançados, Trevo Cel. Av. Jos e A. A. Amarante, São José dos Campos 12.228-001, Brazil

^fSolid State Physics Division, Bhabha Atomic Research Centre, Mumbai 400 085, India

^gYadavindra College of Engineering (YCoE) Punjabi University Guru kashi campus, Talwandi Sabo, Bathinda, Punjab 151302, India

^{*,**} Corresponding authors: rbjotania@gmail.com (Rajshree B. Jotania), ssingh@barc.gov.in (S. S. Meena)

Abstract

Gallium substituted Z-type $\text{Sr}_3\text{Ga}_x\text{Co}_{2-x}\text{Fe}_{24}\text{O}_{41}$ ($x = 0.0 - 2.0$ in steps of 0.4) hexaferrites were synthesised by the sol-gel auto-combustion process, and sintered at 1150 °C. The structural, morphology, magnetic, Mössbauer, dielectric and microwave absorption properties were examined. XRD results of $x = 0.0, 0.4, 0.8,$ and 1.2 samples show the formation of a single Z-type hexagonal phase. The samples $x = 1.6$ and 2.0 show the formation of Z and M phases. Hysteresis loops suggest that samples $x < 1.6$ possess a soft magnetic nature, while the samples $x = 1.6$ and 2.0 show a hard ferrite characteristics. All samples possess multi-domain microstructures. The composition $x = 0.4$ [maximum $M_S = 97.94 \text{ Am}^2\text{kg}^{-1}$] was fitted with seven sextets (Fe^{3+}) and a paramagnetic doublet-A (Fe^{3+}), while beyond $x \geq 0.8$ two more doublets (Fe^{2+}) were observed along with seven sextets in Mössbauer spectra. The maximum values of Fe^{2+} ions (1.26%) and relative area of paramagnetic doublets (1.91%) were observed for $x = 1.6$ composition, which is also responsible for the lowest value of M_S ($69.99 \text{ Am}^2\text{kg}^{-1}$) for this composition. The average hyperfine magnetic field was found to decrease, whereas average quadrupole splitting was found to increase, with Ga-substitution. The substitution of Ga ions enhanced permeability, dielectric constant, magnetic loss and dielectric loss, in a non-linear fashion. The reflection loss was maximum at lower frequencies for samples $x = 0.0$ and 0.8 , and decreases with frequency. Sample $x = 0.8$ has maximum reflection loss of -12.44 dB at 8 GHz, a measured thickness of 3 mm, and a bandwidth of -10

dB at 1.18 GHz. The observed absorption has been discussed with the help of the input impedance matching mechanism and quarter wavelength mechanism. The observed coercivity in different samples also influenced microwave absorption which demonstrated potential in microwave absorber applications.

Keywords: Z-type hexagonal ferrites, Ga-substitution, Mössbauer spectroscopy, Complex microwave properties

Journal Pre-proof

1. Introduction

Recently, the enormous development in wireless technology has created severe electromagnetic pollution from electronic devices operating at high frequency ranges. Due to this pollution, electromagnetic interference (EMI)/radiation affects biological systems and the performance of electronic/electrical devices. Microwave absorbers are used to suppress GHz signals for military aircraft radar in stealth applications [1], and there has been a great deal of research in this area since World War II, particularly in the X-band, which covers around 8.2 to 12.4 GHz. Such materials are characterised by the absorption of electromagnetic waves in the GHz regime, which is determined by their structure, magnetic and dielectric properties [2]. Depending upon the application, these absorbing materials require low reflection loss over the wide/narrow bandwidth [2, 3].

Numerous studies of hexaferrites have been reported for the development of microwave absorbing materials [4] and in this respect; they are superior to cubic spinel ferrites which typically operate in the vicinity of 1 GHz frequency. Hexaferrites are a family of complex ferrites discovered in the late 1950 [5], when they were of interest as microwave materials. The best known hexaferrites are the M-type ferrites (e.g., $\text{BaFe}_{12}\text{O}_{19}$), but owe complex phases too such as the Z-type hexaferrites [6]. These have the chemical composition $\text{A}_3\text{Me}_2\text{Fe}_{24}\text{O}_{41}$ where A represents strontium (Sr), lead (Pb) or barium (Ba), and Me represents a small divalent metal ion (typically a transition metal), a common example being Co^{2+} which typically forms a soft ferrite with high permeability [7]. Z-type Barium ferrites are known to show excellent microwave absorption properties in the low GHz region due to ferromagnetic resonance (FMR) [8-13]. However, this range of frequency can be increased by tailoring the Fe^{3+} substitution with different dopants to have FMR frequencies between 3.5-13.4 GHz [14-18]. The microstructure of the ferrites affect their properties, and flaky Cu and Zn Z-type ferrites containing variable grains showed a good reflection loss of <-10 dB from 2.0 to 9.6 GHz with a minimal of -17 dB reflection loss at ~ 2.5 GHz [14].

The Ba ion can be substituted with Sr to form SrZ-type ($\text{Sr}_3\text{Co}_2\text{Fe}_{24}\text{O}_{41}$) hexaferrite, first reported by Pullar and Bhattacharya [19] produced using the sol-gel process. The formation of monophase Z-type Sr hexaferrite (SrZ) took place over a very narrow temperature range of 1180 to 1220 °C, beyond which it decomposes to form $\text{SrCo}_2\text{Fe}_{16}\text{O}_{27}$ (SrW-phase) [20].

There are hardly any reports accessible in the literature on microwave properties of SrZ-type hexaferrites. High frequency magnetoelectric measurements were carried out on SrZ

[21], looking at the effects of applied voltage on complex permeability at up to 4 GHz with a weak FMR peak between 2.5-3.5 GHz. Recently, $\text{Sr}_3\text{Co}_2\text{ZnFe}_{24}\text{O}_{41}$ was reported to have a reflection loss between -10 to -35 dB over the 8-12.5 GHz range [22], the best samples being 2.6 mm thick. A stable method with precise chemical composition is required for synthesising Z-type hexaferrites, typical techniques including sol-gel, sol-gel auto-combustion, solid-state reactions and chemical co-precipitation [9, 21, 23, 24-30]. A sol-gel auto-combustion process is considered to be one of the best methods, as the metal ions chelation eliminates the elemental homogeneities present in the gels that play a significant part in producing the desired single phase [31, 32].

Ga^{3+} substitution in M-type hexaferrites can enhance the absorption of electromagnetic energy which is appropriate for protective antiradar or EMI shielding from microwave radiation [33]. Trukhanov *et al.* have published several papers on the enhancing effect of Ga substitution on FMR frequencies in barium M ferrites ($\text{BaFe}_{12-x}\text{Ga}_x\text{O}_{19}$) [33-38], and Ihsan Ali *et al.* reported that the series obtained by substituting Cr-Ga in BaM hexaferrites are excellent materials for high-frequency applications [39]. Researchers have studied microwave absorption considering the simulated thickness of the material. For real-world applications as absorbers, EM absorption should be investigated as function of measured/actual thickness of the absorber. However, most of the reported work constitutes absorption investigation as a function of simulated thickness [22, 40, 41].

In the current study, the sol-gel auto-combustion process is used to synthesise $\text{Sr}_3\text{Ga}_x\text{Co}_{2-x}\text{Fe}_{24}\text{O}_{41}$ hexaferrites (where $x = 0.0, 0.4, 0.8, 1.2, 1.6,$ and 2.0), which were then sintered at $1150\text{ }^\circ\text{C}$. This is lower than the usual temperature required to forming the SrZ phase. The main purpose of the current work is to investigate the structural, morphological, magnetic, electrical, impedance and microwave absorbing properties of these $\text{Sr}_3\text{Ga}_x\text{Co}_{2-x}\text{Fe}_{24}\text{O}_{41}$ ($x = 0.0$ to 2.0) hexaferrites when heated at $1150\text{ }^\circ\text{C}$, significantly lower than the usual temperatures required (1180 to $1220\text{ }^\circ\text{C}$), and their suitability for applications like EMI and radar absorbing materials (RAM). This work also considers microwave absorption as a function of the measured thickness.

2. Experimental details

2.1 Synthesis of samples

Fig. 1 represents a flowchart for the synthesis of $\text{Sr}_3\text{Ga}_x\text{Co}_{2-x}\text{Fe}_{24}\text{O}_{41}$ Z-type hexaferrite powder samples. High purity analytical grade strontium nitrate ($\text{Sr}(\text{NO}_3)_2$, 99.0% pure, Loba Chemie), gallium nitrate ($\text{Ga}(\text{NO}_3)_3 \cdot \text{H}_2\text{O}$, 99.9% pure, Sigma Aldrich), cobalt nitrate ($\text{Co}(\text{NO}_3)_2 \cdot 6\text{H}_2\text{O}$, 99.99 % pure, Merck), ferric nitrate ($\text{Fe}(\text{NO}_3)_3 \cdot 9\text{H}_2\text{O}$, 99 % pure, HPLC) and citric acid ($\text{C}_6\text{H}_8\text{O}_7 \cdot \text{H}_2\text{O}$, 99% pure, HPLC) were used as starting materials. According to the stoichiometry of $\text{Sr}_3\text{Co}_{2-x}\text{Ga}_x\text{Fe}_{24}\text{O}_{41}$ hexaferrites, these materials were weighed and dissolved in distilled water to form an aqueous solution. Then, citric acid was added to the solution in a 1:1 molar ratio. Citric acid acts as a chelating agent during the process.

Thereafter, the pH value was adjusted to 7 to neutralise the mixed solution by the dropwise addition of ammonia solution (Merck specialties Private Limited, 25% w/v). The solution was continuously stirred to promote the entire chelation of nitrates with citric acid and the temperature was maintained at 80 °C. Subsequently, the solution got transformed into a viscous brown gel. As the temperature is raised, the gel started to ignite in a self-propagating manner, forming fine powders of a black/dark brown colour. Thereafter, the as-synthesised powders were kept for preheating at 550 °C in air, and then heated at 1150 °C for 5 h in a muffle furnace to obtain Z-type Sr hexaferrite powder.

2.2 Characterisation

Fourier transform infra-red (FT-IR) spectra of sintered samples were measured at room temperature using a Perkin-Elmer LS-55 spectrometer, over the wavenumber range of 400 – 4000 cm^{-1} .

The phase purity and crystal structure of gallium substituted SrZ hexaferrite powder samples were investigated using X-ray diffraction (XRD) with Cu-K_α radiation of 1.5406 Å (Rigaku Geigerflex instrument). Equations 1 and 2 were used to calculate unit cell volume and the crystallite size, respectively, of the prepared Z-type hexaferrites:

$$V_{\text{cell}} = (0.866) a^2 c \quad (1)$$

The average crystallite size of each sample was measured by Scherer's equation:

$$D_{\text{xrd}} = \frac{0.9\lambda}{\beta \cos\theta} \quad (2)$$

where θ = Bragg angle in degree, β = FWHM of the diffraction peak in degree and λ = X-ray wavelength (1.5406 Å).

X-ray density (d_x) was determined using the following formula:

$$d_x = \frac{ZM}{N_A V_{cell}} \quad (3)$$

where M is the molecular mass of $Sr_3Ga_xCo_{2-x}Fe_{24}O_{41}$, Z is the number of molecules per unit cell (Z is 2 here because 1 unit cell contains 2 molecules in Z-type hexaferrites) and N_A is Avogadro's number

Bulk density (d_B) was determined using the following formula:

$$d_B = \frac{m}{\pi r^2 h} \quad (4)$$

where 'r' is the radius, 'h' is the thickness and 'm' is the mass of the pellet.

Porosity (P) was measured using the following expression:

$$P (\%) = \left(1 - \frac{d_B}{d_x}\right) \times 100\% \quad (5)$$

The surface morphology was examined by Carl Zeiss-Auriga field emission scanning electron microscope (FE-SEM).

Magnetic hysteresis loops were measured for $Sr_3Ga_xCo_{2-x}Fe_{24}O_{41}$ hexaferrites at room temperature using a SQUID magnetometer, Quantum Design, MPMS5 with an applied field of 4T.

A conventional spectrometer operating in constant acceleration mode in transmission geometry with Co^{57} source in Rh matrix of 50 mCi was used to record Mössbauer spectra. These spectra were fitted using the WinNormos site fit program. An enriched $\alpha\text{-}^{57}Fe$ metal foil was used to calibrate the velocity scale. The isomer shift values are relative to Fe metal foil ($\delta = 0.0$ mm/s). The dependence of quadrupole splitting (Δ) with Ga-substitution in $Sr_3Ga_xCo_{2-x}Fe_{24}O_{41}$ hexaferrites provides information on the change in the type of magnetic anisotropy, namely c-axis anisotropy (if $\langle\Delta\rangle$ positive) and c-plane anisotropy (if $\langle\Delta\rangle$ negative)]. The relation of quadrupole splitting with the angle θ between the direction of hyperfine fields (internal magnetic field) and the principal axis of Electric Field Gradient (EFG) is given by[42]:

$$\Delta = \frac{1}{4} e q Q (3 \cos^2 \theta - 1) \quad (6)$$

where, q is the z component of the EFG along the principal axis and Q is the nuclear quadrupole moment.

The dielectric measurements of all samples were implemented in the frequency range of 100 Hz to 2 MHz at room temperature by using a Precision LCR meter, Agilent E4980 A.

The dielectric constant (ϵ') of the samples was measured using the following relation:

$$\epsilon' = \frac{C_p t}{\epsilon_0 A} \quad (7)$$

where, ϵ_0 is the permittivity of the free space, A is the cross-sectional area of the electrode, t is the thickness of pellets and C_p = capacitance

The ratio between ϵ'' (the imaginary dielectric constant) and ϵ' (the real dielectric constant) depicts the dielectric loss tangent ($\tan \delta$):

$$\tan \delta = \frac{\epsilon''}{\epsilon'} \quad (8)$$

The AC conductivity of all samples was measured using the formula:

$$\sigma_{ac} = \frac{2\pi f t C_p \tan \delta}{A} \quad (9)$$

The electrical modulus (M) in terms of resistive (real i.e. M') and reactive (imaginary i.e. M'') parts can be expressed as:

$$M = M' + M'' \quad (10)$$

$$\text{where, } M' = \frac{\epsilon'(\omega)}{[\epsilon'(\omega)]^2 + [\epsilon''(\omega)]^2} \text{ and, } M'' = \frac{\epsilon''(\omega)}{[\epsilon'(\omega)]^2 + [\epsilon''(\omega)]^2}$$

The maxima in M'' occur when the following condition is satisfied:

$$\omega \tau = 1 \quad (11)$$

where, ω (angular frequency) = $2\pi f_{\max}$ and τ = relaxation time

High-frequency complex permeability and permittivity measurements were performed over the microwave frequency region of 8-12.5 GHz using an Agilent N5231 PNA-L Microwave Network Analyser with a coaxial termination and an APC-7 connector as a sample holder.

The reflection loss (RL) of a single layer absorber is measured with the aid of transmission line theory using the following relation:

$$RL = 20 \log \left| \frac{(Z_{in} - Z_0)}{(Z_{in} + Z_0)} \right| \quad (12)$$

where, Z_{in} = input impedance of a metal backed absorber, and $Z_0 = 377 \Omega$ is the characteristic impedance of free space

Z_{in} is written as:

$$Z_{in} = Z_o \sqrt{\frac{\mu^*}{\epsilon^*}} \tanh \left[j \left(\frac{2\pi f t_m}{c} \right) \sqrt{(\mu^* \cdot \epsilon^*)} \right] \quad (13)$$

where, t_m is thickness, f is frequency, ϵ^* is complex permittivity, μ^* is complex permeability and c denotes velocity of light

Complex permittivity, complex permeability can be expressed by:

$$\mu^* = \mu' - j\mu'' \quad (14)$$

where, μ' = the real permeability, μ'' = the imaginary permeability, and $j = \sqrt{-1}$.

$$\epsilon^* = \epsilon' - j\epsilon'' \quad (15)$$

where, ϵ' = the real dielectric constant and ϵ'' = the imaginary dielectric constant.

Both real and imaginary dielectric constants and magnetic permeabilities contribute to dielectric and magnetic losses and absorbing behaviour in the material.

Mathematically, matching thickness (t_c) can be expressed as:

$$t_c = \frac{nv}{4f\sqrt{|\mu^* \epsilon^*|}} \quad (16)$$

where, n is an integer 1, 3, 5..... and v denotes velocity of light

3. Results and Discussion

3.1. FTIR Analysis

FT-IR spectra of heated samples are shown in Fig. 2 (a) $x= 0.0$ and 0.4 samples depict two characteristic peaks around 600 and 415 cm^{-1} , while $x > 0.4$ shows three characteristic vibration peaks in the ranges of $400\text{-}430 \text{ cm}^{-1}$, $530\text{-}550 \text{ cm}^{-1}$ and $590\text{-}620 \text{ cm}^{-1}$, respectively, ascribed to octahedral and tetrahedral clusters, which confirms the presence of Fe-O stretching bands. The characteristic peaks present at $400\text{-}430 \text{ cm}^{-1}$ wavenumbers indicate the vibrations of octahedral clusters, while the other two peaks depict the tetrahedral bonds [1, 43, 44]. The vibrations of octahedral (ν_2) and tetrahedral (ν_1) metal-oxygen bonds with respect to x are presented in Fig. 2 (b). The difference between the tetrahedral and octahedral band positions is expected, as vibrational modes of tetrahedral clusters are higher than those of octahedral clusters, because tetrahedral clusters have shorter bond lengths [45]. The characteristic bands were observed to be shifted to a lower wavenumber as Ga substitution increases. This is because Ga ions (69.723 amu) have a greater atomic weight than Co ions

(58.933 amu), and the wavenumber is inversely proportional to the atomic weight [46]. There were no other characteristic bands present, which confirms that all the organic compounds were completely eliminated.

3.2. XRD Analysis

The X-ray diffraction patterns of all samples are displayed in Fig. 3(a) and Fig. 3 (b). Bragg peaks were identified using WINPLOTR software, and the obtained peaks were analysed with standard data (JCPDS file no. 19-0097; $a = b = 5.88 \text{ \AA}$, $c = 52.31 \text{ \AA}$ and $V = 1566.28 \text{ \AA}^3$, space group $P6_3/mmc$) of the Z-type hexaferrite crystal structure.

The highly intense X-ray diffraction peak corresponding to (h k l) value (1 0 16) is viewed at $2\theta \sim 32^\circ$ in samples $x = 0.0, 0.8$ and 1.2 (Fig. 3(a)), providing clear evidence for the formation of single Z-phase, which matches well with the standard parameters (JCPDS #19-0097). However, after substituting Ga in the initial $x = 0.4$ sample (Fig. 3(a)), the highest intensity peak was observed at $2\theta \sim 34^\circ$ indexed with a (h k l) value of (1110). Nevertheless, the peak positions all matched that for Z ferrite. The shifting of the highest intensity peak in the $x = 0.4$ sample, could be attributed to a texturing effect through the alignment of hexagonal grains in this sample [47]. With further substitution for $x = 0.8$ and 1.2 , the high intensity peak was indexed to single Z-phase at $2\theta \sim 32^\circ$, suggesting any texture effects were only present with the lowest level of Ga substitution. Thereafter, in samples $x = 1.6$ and 2.0 samples (Fig. 3(b)), the SrM-phase ($\text{SrFe}_{12}\text{O}_{19}$, standard JCPDS card no. 72-0739; $a = b = 5.78 \text{ \AA}$ and $c = 22.98 \text{ \AA}$) was found to co-exist with the Z phase, shown by the strong peak at $\sim 34^\circ$ with (h k l) value of (1 1 4).

SrZ hexaferrites has a very narrow range of formation, normally forming at around $1180 \text{ }^\circ\text{C}$, and it easily decomposes to W-type hexaferrite above $1200 \text{ }^\circ\text{C}$. The M phase, SrM in the case of SrZ, always forms as a precursor to the Z phase between $800\text{-}1000 \text{ }^\circ\text{C}$, depending on the preparation method used [7]. In the current work, all the samples were heated at $1150 \text{ }^\circ\text{C}$ in order to attempt to obtain a pure Z-phase, and to avoid the evolution of the W- phase. This unusually low temperature appears to have been successful for the formation of a pure Z phase for the unsubstituted Z ferrites and with Ga levels of $x = 0.4\text{-}1.2$, using the sol-gel auto-combustion process. At higher substitution levels ($x = 1.6\text{-}2.0$), the co-existence of the SrM phase suggests that full conversion to the Z phase had not been achieved, and it seems that some higher temperature is required with this amount of added Ga.

Table 1 represents the unit cell volume, full width at half maximum (FWHM), c/a ratio, average crystallite size and lattice constants with gallium substitution (x). The variation of unit cell volume (V), lattice parameters ($'a'$, $'c'$) and aspect ratio (c/a) with respect to gallium substitution in SrZ hexaferrites is shown in Fig 3(c). All three parameters exhibit a decreasing tendency with increasing substitution of Ga, and this is because the ionic radius of Ga^{3+} (0.62 Å in 6-coordination) is less than that of Co^{2+} (0.75 Å) [47]. Table 1 and Fig. 3 (c) clearly indicate that the decrease of $'a'$ is lower than that of $'c'$ and typically hexaferrites show more variation in the basal-plane hexagonal $'c'$ axis [48]. The values of c/a ratio as observed in Fig. 3 (c) falls in the usual range of 8.86-8.89 [16], and slowly increased (from 8.866 to 8.881) with Ga-substitution, meaning that the crystal symmetry is not greatly altered by Ga substitution. The crystallite size of samples $x = 0.0$ to 1.6 increase from 22.56 nm to 30.08 nm, and further decrease to 23.83 nm for $x = 2.0$ sample.

3.3. Physical Properties

Density and porosity are considered to be crucial aspects in regulating the physical properties of polycrystalline ferrites. The role of Ga substitution on bulk density, X-ray density and porosity is represented in Fig. 4 and Table 2.

As Ga substitution increases, the X-ray density of all samples increases from 4.95 to 5.03 g/cm^3 . Equation 3 clearly depicts that the X-ray density depends on molecular weight, as it is directly proportional to the $'c'$ parameter, while it is inversely dependent on cell volume. The decrease in $'c'$ parameter with rising Ga content and the larger molecular weight of Ga (69.723 au) compared to Co (58.933 au) are mainly responsible for the increase in values of X-ray density [49]. However, the bulk density shows a decreasing trend and porosity was found to increase, which is at least partly because of the low density of Ga (5.9 g/cm^3) in comparison with its host Co (8.86 g/cm^3) [50]. This decreasing trend of bulk density is also ascribed to the increase in intra-granular porosity that results from discontinuous grain growth [51]. The values of bulk density are low as compared to X-ray density. This is due to cracks and pores present on the microscopic and macroscopic scale, and also due to the existence of vacancies in the lattice on the atomic scale [50]. As would be expected, the trend in porosity is observed to be opposite to that of bulk density. The unsubstituted sample $x = 0.0$ has the lowest porosity and the highest bulk density; however, the changes are not exactly linear and $x = 0.8$ has the maximum porosity and minimum bulk density.

3.4. Surface Morphology

Fig. 5 represents the FE-SEM micrographs of $\text{Sr}_3\text{Co}_2\text{Fe}_{24}\text{O}_{41}$, $\text{Sr}_3\text{Co}_{0.8}\text{Ga}_{1.2}\text{Fe}_{24}\text{O}_{41}$, and $\text{Sr}_3\text{Ga}_2\text{Fe}_{24}\text{O}_{41}$ hexaferrite powders heated at 1150 °C for 5 h. Their shape shows platelet type morphology, typical of hexaferrites. The unsubstituted sample ($x = 0.0$) shows a different size distribution of the particles and sample $x = 1.2$ shows the increase in the agglomeration of grains. Sample $x = 2.0$ shows the evolution of well-crystallized hexagonal plates along with the big cluster of agglomerated grains. Evidently, agglomeration of grains creates empty space in the form of porosity in all Ga substituted samples. This variation depicted in micrographs is consistent with porosity and density variation of the samples as listed in Table 2.

3.5. Magnetic Properties

3.5.1. Hysteresis loops

Fig. 6(a) represents the magnetic hysteresis loops of $\text{Sr}_3\text{Co}_{2-x}\text{Ga}_x\text{Fe}_{24}\text{O}_{41}$ ($x = 0.0, 0.4, 0.8, 1.2, 1.6$ and 2.0) hexaferrites. The individual hysteresis loop of the $x = 0.8$ sample is also presented in Fig. 6 (b). The values of remanant magnetisation (M_r), coercivity (H_c), saturation magnetisation (M_s), and squareness ratio (M_r/M_s) are obtained from the hysteresis loops and are tabulated in Table 3, and their variation with x is depicted in Fig. 6(c).

For the unsubstituted $x = 0.0$, the values of remanant and saturation magnetization were found to be $0.1 \text{ A m}^2\text{kg}^{-1}$ and $80.27 \text{ A m}^2\text{kg}^{-1}$, respectively. This M_s is much higher than that usually reported for SrZ, which typically has M_s of around $50 \text{ A m}^2\text{kg}^{-1}$ [7, 19, 20]. The XRD data, along with the extremely soft, narrow loop and low H_c demonstrate that this sample contains no M phase. There was also no trace of magnetite (Fe_3O_4) in the XRD pattern - this is a soft spinel ferrite with a high M_s of around $90 \text{ A m}^2\text{kg}^{-1}$, but it would not be expected to be present in large quantities after heating to 1150 °C in air, as the Fe^{2+} is oxidised. It is possible that there could be some SrW ($\text{SrCo}_2\text{Fe}_{16}\text{O}_{27}$) phase present [52, 53], and studies of SrW-type hexaferrites show higher M_s values around $67\text{-}73 \text{ A m}^2\text{kg}^{-1}$ [54], although it was not identified in XRD analysis. SrW normally appears as a decomposition product of SrZ above 1200 °C [8], and does not usually form at temperatures as low as 1150 °C [54], although the samples prepared here have formed the Z phase at a lower than usual temperature. High M_s values of around $80 \text{ A m}^2\text{kg}^{-1}$ were reported for Sm^{3+} substituted BaZ [55]. For now the anomalously high M_s value of this seemingly single phase SrZ ferrite is unexplained, and the product of this synthesis route requires further study in the future.

The values of M_S for samples after Ga substitution are in the range of 69-98 $\text{Am}^2\text{kg}^{-1}$ with the highest M_S value of 97.94 $\text{A m}^2\text{kg}^{-1}$ being observed for sample with $x = 0.4$. Only samples $x = 0.8$ and 1.6 have M_S values below 80 $\text{A m}^2\text{kg}^{-1}$. The variation in M_S and its higher values for $x = 0.4, 1.2$ and 2.0 compositions and lower values of M_S for $x = 0.8$ and 1.6 compositions have been explained in details in the next section by Mössbauer spectroscopy.

For values of substitution x between 0.0-1.2, all of the samples are soft ferrites, with extremely low H_C and M_r values, although these do increase slightly with increasing Ga substitution. Sample $x = 1.2$ has significantly (although still very low) values of $H_C = 18.47$ kA m^{-1} (~ 300 Oe) and $M_r = 12.3$ $\text{A m}^2\text{kg}^{-1}$. The individual loop of the $x = 0.8$ sample is presented in Fig. 6 (b), where it can be observed that it is an extremely soft ferrite ($H_C \sim 4$ kA m^{-1}). The irregular change in magnetisation at an applied field of around 0.5 T is typical for SrZ ferrites, and was first studied by Pullar *et al.* [19, 56]. This is not due to an impure phase, but is due to a change in the magnetic phases, and is associated with the magnetic non-collinear spin structures which give rise to multiferroicity / magnetoelectricity in these ferrites [7, 57]. The existence of this behaviour in the Ga substituted SrZ attributes that this is also probably multiferroic ferrite at room temperature, and it also confirms that the samples are SrZ ferrite, despite their unusually high M_S values.

For $x = 1.6$ and 2.0 samples, the existence of the precursor SrM phase was observed by XRD. It is also supported by the hysteresis loops, which become much wider as a hard ferrite is formed – a mixture of the soft Z and hard M phases: H_C increases to 94.53 and 186.87 kA m^{-1} (1185 and 2342.55 Oe), and M_r to 24.76 and 36.38 $\text{A m}^2\text{kg}^{-1}$, respectively. The aspect ratio (c/a) of prepared Z-type hexaferrites increases with an increase in Ga^{3+} content as seen in Fig. 3(c). This increase in c/a is responsible for the continuous rise in the H_C because the magnetic moments in these Ga^{3+} substituted hexaferrites ($x \geq 0.8$) are in the c -axis, due to which magnetic anisotropy increases as the easy axis of magnetisation shifts from the c -plane to the c -axis [58]. Thus, the high value of H_C for $x = 1.6$ and 2.0 clearly depicts that the prepared hexaferrites are hard magnetic materials. Coercivity primarily depends upon anisotropy field (H_a) and microstructure: it varies in direct proportion with H_a and inversely with porosity. The anisotropy field has been calculated from hysteresis loops by the law of saturation [59].

Fig. 6 (c) displays an increase in H_a from 917 kA m^{-1} to 1807 kA m^{-1} with the substitution of Ga from $x = 0.4$ to 2.0, and H_C also follows the same trend from 0.46 kA m^{-1} to

186.87 kA m⁻¹ in the same samples. However, the trend of H_C and H_a is not the same for samples $x = 0.0$ to 0.4 at lower substitution level: H_C and H_a increases and decreases respectively from sample $x = 0.0$ to 0.4 . The substantial increase in porosity attributes to the rise in H_C among the same sample. The very low H_a value for $x = 0.4$ would also be typical of a textured sample with the alignment of platy hexagonal grains, as possibly observed in the XRD data for this sample. Such texturing can also result in an enhancement in magnetisation values.

The anisotropy field (H_a) depends on the occupancy of Fe³⁺ ions in $4f_2$ (spin down) and 2b sites (spin up) [60]: $4f_2$ sites are more numerous than 2b sites, and the very low value of H_a implies that Fe³⁺ ions can be replaced by Ga³⁺ ions in a greater number of $4f_2$ sites. Since the mechanism of magnetisation depends upon different magnetic moments in spin up and spin down sites [$M_S = M$ (spin up) - M (spin down)], M_S should increase in $x = 0.4$ due to greater occupancy of spin down sites by the substitution of poorly magnetic Ga³⁺ ions. The highest M_S in $x = 0.4$ as shown in Fig. 6 (c) is consistent with the explanation of H_a .

The squareness ratio (M_r/M_s) also increases as the ferrites become harder, but is below 0.5 for all samples, and confirms the formation of multidomain structures [61].

3.5.2. Mössbauer analysis

Mössbauer spectroscopy is an outstanding experimental tool to interpret the magnetic properties of ferrites. It provides information on the ionic states (Fe³⁺ or Fe²⁺) and spin states (high spin, low spin) of Fe-ions in octahedral and tetrahedral interstices, cation distributions, variations from stoichiometry and types of ordering. Thus, this technique is becoming a general tool in ferrite technology [62, 63].

Fig. 7 shows the Mössbauer spectra of all samples, and the results of analysis are given in Table 4. Mössbauer spectra of the un-substituted sample ($x = 0.0$) were fitted well with six sextets (Zeeman splitting patterns) and a paramagnetic doublet-A, while the $x = 0.4$ composition was fitted with seven sextets and a paramagnetic doublet-A. After $x \geq 0.8$ compositions, two more doublets were also observed, labelled as doublet-B and doublet-C, along with seven sextets. Fig. 8 (a-h) shows the variation of different parameters with Ga-substitution (x), such as isomer shift (δ), average isomer shift ($\langle\delta\rangle$), hyperfine magnetic field, average hyperfine magnetic field ($\langle H_{hf}\rangle$), quadrupole splitting (Δ), average quadrupole

splitting ($\langle\Delta\rangle$), relative area of Fe^{3+} and Fe^{2+} (%), and relative area of sextets (ferrimagnetic) and doublets (paramagnetic). The values of isomer shift represent the chemical state of the Fe-ions in the Ga-substituted Z-type hexaferrites. There are ten crystallographic sites [six-octahedral sites $\{12k_{\text{VI}}(\uparrow), 4f_{\text{VI}}(\downarrow), 4e_{\text{VI}}(\downarrow), 4f_{\text{VI}}^*(\uparrow), 12k_{\text{VI}}^*(\uparrow), \text{ and } 2a_{\text{VI}}(\uparrow)\}$, three tetrahedral sites $\{4e_{\text{IV}}(\downarrow), 4f_{\text{IV}}(\downarrow) \text{ and } 4f_{\text{IV}}^*(\downarrow)\}$, and a five-fold site of $2d_{\text{V}}$] in Z-type hexaferrites, having space group $P63/mmc$. The Fe, Co and Ga ions were found to be located at these ten sites [64]. The total numbers of cations ($\text{Fe}^{3+}/\text{Fe}^{2+}$, Co^{2+} , and Ga^{3+}) are 26 in the present SrZ hexaferrites. Five types of site have spin up (16 Fe/Co-ions) and five types of site have spin down (10 Fe/Co-ions) directions of magnetic moment. Here, magnetic properties depend on occupancy and ionic states of these ions.

The sextet F ($\delta_{\text{oct}} = 0.357 \text{ mm/s}$, $H_{\text{hf}} = 39.5 \text{ Tesla}$), which maybe belongs to $4f_{\text{VI}}$ Octahedral site (spin down) along with other sites, had a relative area of nearly 39.7%. In the sample $x = 0.4$; this sextet F further converted into two sextets (F and G) with relative areas of 23% and 14%, respectively. So, there is a drastic reduction in the relative area of sextet F (spin down) and a sudden increase in (spin up) tetrahedral sites in the form of sextet-G ($\delta_{\text{tet}} = 0.166 \text{ mm/s}$, $H_{\text{hf}} = 41.1 \text{ Tesla}$), which may lead to an increase in the M_{S} value for $x = 0.4$. Sample $x = 0.8$ is the less dense and most porous sample, which will affect M_{S} , and $x = 1.6$ is a mixture of M and Z phases so the results of M_{S} may alter here. This is also well known that the Z-type hexaferrites are ferrimagnetic materials (16Fe-ions have spin up and 10Fe-ions spin down directions). The higher values of M_{S} in the other three samples; $x = 0.4, 1.2$ and 2.0 , are also due to the occupancy of Ga-ions at spin down sites, and the low percentage of paramagnetic ions confirmed from the Mössbauer spectra. The variation in the relative percentage of sextets (ferrimagnetic components) and paramagnetic doublets with Ga-substitution are shown in Fig. 8h. The total paramagnetic components are found to increase with Ga-substitution, which effects and reduce the value of M_{S} . The percentage of Fe^{3+} ions decreases, whereas Fe^{2+} ions increase with increasing Ga-substitution, and a maximum (Fe^{2+} ions of doublets = 1.26%) for $x = 1.6$ composition (Fig. 8g). This composition is also having a maximum relative area of paramagnetic doublets (1.95%), and one of the sextet-D has a higher isomer shift value (0.73 mm/s) due to ($\text{Fe}^{3+} + \text{Fe}^{2+}$) ions (Fig. 8a). This means some of the Fe^{3+} ions are converted into Fe^{2+} ions in this sextet, and we know that the magnetic moment of Fe^{3+} ions $>$ Fe^{2+} ions. These two factors (maximum relative area of paramagnetic doublets and maximum Fe^{2+} ions in paramagnetic and magnetic state) are responsible for the lowest value of M_{S} of this composition ($x = 1.6$). The value of M_{S} will be reducing when the

percentage of ferrimagnetic components reduce and the percentage of paramagnetic components increase, as shown in Fig. 8h. The variation in M_S is exactly following this rule for $x \geq 0.8$ samples.

Fig. 8(b) shows the relation between the averaged isomer shifts with Ga-substitution. The isomer shift values of sextets for all samples were found to be in the range of 0.134 – 0.575 mm/s (except sextet D of $x= 1.6$ composition) (Table 4 and Fig. 8a). These values are the typical values of Fe^{3+} with high spin state [65-68]. The δ value of sextet D for composition $x= 1.6$ is found to be 0.73 mm/s, that confirms the more Fe^{2+} ions along with Fe^{3+} ions at this site [67, 68]. When the relative percentage of Fe^{3+} and Fe^{2+} ions are equal at a site for the sextet, as in Fe_3O_4 spinel ferrite, for the octahedral site then the value of δ_{oct} is between 0.5-0.65 mm/s [69-71]. However, in the present case, the value of δ is higher, meaning that this site has more Fe^{2+} than Fe^{3+} ions. The isomer shift for the octahedral site (δ_{oct}) is greater than that of the tetrahedral site (δ_{tet}), which helps to identify the different Fe-sites [72-74]. The isomer shift values of doublet-A for all samples are found to be between 0.136 to 0.33 mm/s, which is also indicating a Fe^{3+} high spin state [65-68, 75, 76]. The values of δ for doublet-B in samples $x \geq 0.8$ are found to be between 1.41-1.89 mm/s (Fe^{2+} high spin). These values belong to Fe^{2+} ions in high spin state at octahedral sites [65-68]. The values for doublet-C in samples $x \geq 0.8$ are between 0.39-0.605 mm/s ($\Delta E_Q = 4.78-4.92$ mm/s, Fe^{2+} low spin state) [77]. The variation in the relative area of Fe^{2+} and Fe^{3+} ions with increasing the Ga-substitutions is shown in Fig. 8 (g). There is no presence of Fe^{2+} ions in $x \leq 0.4$ compositions. As x increases ($x \geq 0.8$), there is a small amount of Fe^{2+} ions ($x = 0.8$, 0.4% Fe^{2+} ions) present in these compositions and the percentage of Fe^{2+} ions increases with Ga-substitution. This suggests that beyond $x \geq 0.8$ compositions the Ga^{3+} begins to substitute not only for Co^{2+} , but also at some Fe^{3+} sites and trying to balance the charge in the system the substituted Fe^{3+} will in turn reduce to Fe^{2+} and reside in the Co^{2+} sites. The existence of these Fe^{2+} ions increases greatly up to $x = 1.6$ composition (1.26%), and then slightly decreased for $x = 2.0$ (1.1%), with the decrease between these two possibly being attributable to the existence of more of the SrM phase with $x = 2.0$.

Fig. 8(e) shows the decreasing nature of the average hyperfine field ($\langle H_{hf} \rangle$) with Ga-substitution. The decrease in $\langle H_{hf} \rangle$ is attributed to the decrease in the exchange interactions, and also to the weak interaction between the non-magnetic ions (Ga) and magnetic ions (Fe/Co) in sub-lattices [78]. The SrM phase is also present in $x = 1.6$ and 2.0 compositions, reducing the overall contribution of the Ga-Co interactions. The relative area of doublets also

increases with Ga-substitution. These aspects also account for the decrease in M_S and H_{hf} with Ga-substitution.

Fig. 8(f) shows the compositional dependence of averaged quadrupole splitting ($\langle\Delta\rangle$) which gives information on the variation in magnetic anisotropy i.e c-axis and in-plane anisotropy. The value of $\langle\Delta\rangle$ was found to be increased with the Ga-substitution due to structural and magnetic distortion, which also confirmed the decreasing trend in the magnetic anisotropy. The magnetic moment of Fe^{3+} -ions are either in the c plane or along the c axis, $\langle\Delta\rangle$ will have significantly different sign and magnitude due to different θ value in Equation 6. The increasingly positive value of $\langle\Delta\rangle$ (Fig. 8f) of $Sr_3Co_{2-x}Ga_xFe_{24}O_{41}$ hexaferrites indicates that the magnetic anisotropy is progressing towards the c-axis with Ga-substitution [42, 64, 75], meaning that the angle of the cone of magnetisation to the c-axis found in unsubstituted SrZ hexaferrite will probably becoming smaller, and as a result H_C will also increase for Ga-substituted samples [79]. The magnetic anisotropy of $Sr_3Co_{2-x}Ga_xFe_{24}O_{41}$ hexaferrites is modified from the c plane to c axis orientation at $x = 0.4 - 0.8$. We have also observed similar types of trend for $\langle H_{hf} \rangle$, $\langle\Delta\rangle$, and relative area of Fe^{2+} ions with increasing the Ga-substitution in our previous studies on Z type hexaferrites $Sr_3Co_{2-x}Ga_xFe_{24}O_{41}$ synthesized at 1200 °C [79].

3.6. Dielectric measurement at low frequency (100Hz-2MHz)

The dependence of dielectric constant (ϵ') and loss tangent ($\tan \delta$) are presented in Fig. 9 (a and b). The values of dielectric constant are high ($\epsilon' > 20$) in the low-frequency range (Fig. 9 (a)), and it decreases as frequency increases to 2 MHz. The high dielectric constant observed at low frequency is attributed to the dislocations, voids and defects existing in the crystal structure. The varying dielectric constant with frequency is ascribed to the space charge polarisation, which depicts the inhomogeneous dielectric structure, as described by Maxwell-Wagner in correspondence with Koop's phenomenological theory [80].

When the frequency further rises beyond a certain point, the polarisation decreases because the movement of dipoles cannot follow the alternating field. It levels out to more-or-less constant values above ~500 kHz. In the low-frequency regime, there is a non-linear fall in ϵ' with the substitution of Ga. The substitution renders (i) increase in grain size easing the flow of charge carriers (ii) increases porosity and reduces bulk density impeding the flow of charge carriers (iii) decreases Fe^{3+} reducing the hopping between charge carriers Fe^{3+} and Fe^{2+} ions. These factors altogether cause non-linear ϵ' in the samples. The main

mechanism of electrical conduction in ferrites at room temperature is electron hopping between Fe^{2+} and Fe^{3+} ions, unlike in polarisation, which will typically increase with frequency [81]. Above $x = 0.4$, the increase in x leads to an increase in Fe^{2+} ions and an increase in conduction will lead to increased dielectric losses ($\tan \delta$) as well.

As observed in Fig. 9(b), the trend in dielectric losses is quite similar between all samples, but those with $x > 0.4$ tend to show slightly greater losses. The dielectric loss tangent is based on types and number of charge carriers, structural homogeneity, stoichiometry, Fe^{2+} content, heating temperature and composition [82, 83]. The high values of loss tangent are high in the low-frequency region as higher energy is required for electron exchange between Fe^{2+} and Fe^{3+} ions that is induced by the high resistance of grain boundaries. As frequency increases, less energy is needed for electron exchange due to the low resistivity of conductive grains and, therefore, the observed value of $\tan \delta$ is low [84]. The loss peak appears when the frequency of the applied ac field matches with the jumping frequency of electrons between Fe^{2+} and Fe^{3+} [85]. $\text{Sr}_3\text{Co}_2\text{Fe}_{24}\text{O}_{41}$ ($x = 0.0$) show a loss peak at ~ 1.2 kHz, and most of the other samples are similar, except for $\text{Sr}_3\text{Co}_{1.6}\text{Ga}_{0.4}\text{Fe}_{24}\text{O}_{41}$ ($x = 0.4$) with a higher loss peak at ~ 13.3 kHz. The increased permittivity in this sample is between 1-10 kHz and this higher loss peak could be due to microstructure differences as discussed earlier. We suspect that sample maybe textured and this sample also has the highest M_S value.

Generally, the electrical conductivity in ferrites is due to the hopping of electrons between the ions of the same element that exists in more than one valence state, and is assigned arbitrarily over crystallographically identical sites [86], e.g. when Fe^{3+} and Fe^{2+} coexists in the same site. The variation of AC conductivity (σ_{ac}) with frequency is represented in Fig. 9(c). The AC conductivity is found to increase with an increase in frequency, and samples show relatively large dispersion at low frequency regimes. According to Maxwell-Wagner's theory, the grain boundaries are more effective in low frequency region, which impedes the electron hopping among Fe^{3+} and Fe^{2+} ions. The conductive grains become more active with the increasing frequency, and encourage the hopping of the electron between Fe^{3+} and Fe^{2+} ions. The sample with $x = 0.4$ shows a significantly higher conductivity above 10 kHz, where it also had a peak in $\tan \delta$.

3.7. Frequency-dependent impedance (100 Hz-2 MHz)

Studying the nature of a material's response to an applied a.c. field along with the impedance behavior helps to understand the grain and grain boundary relaxation process. Fig.10 (a) represents the real part of impedance (Z') with the applied frequency and Fig. 10 (b). shows the complex part of impedance (Z'') with the applied frequency of $\text{Sr}_3\text{Co}_{2-x}\text{Ga}_x\text{Fe}_{24}\text{O}_{44}$ ($x = 0.0, 0.4, 0.8, 1.2, 1.6, 2.0$) hexaferrites.

The impedance decreases as frequency increases, and the curves of all samples merge at frequencies above 1 kHz, and approach near to zero which, indicates a frequency-independent phenomena. This minimum level is associated with the possibility of space charge generation and a decrease in energy barrier [87, 88]. The relaxation time decreases as frequency increases, resulting in the rapid recombination of space charge. This decrease in space charge polarisation with increasing frequency leads to the intermixing of curves [89].

The relaxation peak present in samples with $x = 0.4$ and 2.0 , as seen in Fig. 10 (b), depicts the hopping of electrons at lower frequencies (inset of Fig. 10 b). These relaxation peaks observed at lower frequencies suggest the possible generation of oxygen vacancies during the hopping of electrons.

3.8. Complex modulus analysis (100 Hz-2 MHz)

Electric modulus analysis is applicable to understand the electric characteristics of materials like ion hopping rates, conductivity relaxation time, etc. The study of relaxation behaviour and grain-grain boundary contribution to total conductivity of a material is carried out using the complex electric modulus.

Fig.11 (a) represents the real part of dielectric modulus (M') with frequency and substitution of Ga causes a non-linear increase in M' . The M' values are very small in the lower frequency region as observed in Fig. 11 (a) and M' increases with frequency, attaining a maximum value at 2 MHz. The induced electric field reduces the restoring force controlling the mobility of charge carriers, which are responsible for the rise in M' . The small value of restoring force supports the conduction mechanism in hexaferrites and it increases the conductivity with the increasing frequency, which is in agreement with conductivity graphs [Fig. 9 (c)] [90]. It can be seen that M' is significantly greater at higher frequencies (> 10 kHz) for $x = 1.6$ and 2.0 , the samples with SrM as a second phase. It is evident from the plots

that samples have nearly zero value of M' in the low-frequency regime, which signifies the negligible electrode polarisation in the samples [91, 92].

Fig.11 (b) represents the variation of an imaginary part of dielectric modulus (M'') with frequency. The distinct peaks found in all samples are associated with the dielectric relaxation as well as the mobility of charge carriers that leads to the hopping of electrons from one site to another. The frequency region beneath the maximum peak represents the mobility of charge carriers over long range. The frequency region over the maximum peak depicts the mobility of charge carriers over short distances as charge carriers are constrained to potential wells [93].

It can be seen that for $x = 0.4$ the long-range charge mobility continues to much higher frequencies, perhaps suggesting that inter-grain conduction mechanisms are more favoured in a textured sample, with aligned planar crystal faces in contact. This could also explain why it lacks the lower frequency ϵ' peak at ~ 1 kHz observed in the other samples.

3.9. Cole-Cole plot

The Cole-Cole plot depicts the interfacial polarisation effect, separating the grain and grain boundary contributions. The Cole-Cole plot using real (M') and imaginary modulus (M'') is shown in Fig. 12. Two semicircular arcs are observed in all the samples: The left-hand semicircle at the low-frequency part depicts the grain boundary contributions [94], whereas the right-hand semicircle is associated with the grain resistance for high frequency [95]. The centre of semi-circular arcs lies above M' -axis implying Debye relaxation in the samples.

3.10. Complex permittivity and permeability at high frequency (X-band, 8GHz-12.5 GHz)

Fig. 13 (a, b, c and d) presents the dielectric constant (ϵ') and imaginary dielectric constant (ϵ''), real permeability (μ') and imaginary permeability (μ'') of the $\text{Sr}_3\text{Co}_{2-x}\text{Ga}_x\text{Fe}_{24}\text{O}_{41}$ ferrites between 8 GHz-13 GHz. There is an observation of a non-monotonic increase in ϵ' , ϵ'' , μ' and μ'' with the substitution of Ga ions. The resonance or dielectric relaxation is seen in samples $x = 0.4, 1.2$ and 1.6 after 10 GHz. The dielectric loss in samples $x = 0.0, 0.8, 2.0$ depicts nearly frequency independent nature. It can be seen from the plots that sample $x = 1.6$ has a negative peak in μ'' and it is 180° out of phase with respect to the ϵ'' peak. Therefore, total loss does not oscillate with frequency, and this variation is attributed to measurement uncertainty. Similar variations were observed by Handoko *et al.* in Co-Zn doped Barium

hexagonal ferrite, when μ'' and ε'' were in anti-phase with each other [96]. The large dispersion is seen in μ'' for samples $x = 0.0, 0.4$ and 0.8 , and it decreases with frequency. There is not any significant change to be discussed in μ' and μ'' with substitution in the rest of the samples.

3.11. Reflection Loss (Microwave Absorption)

The reflection loss (RL) determines the absorbing properties of materials with electromagnetic waves. The wave transmissivity of materials has an enormous effect on absorbing properties. It suggests that when electromagnetic waves are incident on the surface of a material and it enters to its deepest part, then the attenuation of the electromagnetic wave takes place and a wave is absorbed by absorber efficiently. Hence, the lower the value of RL, the better will be the capability for the absorption of those frequencies by the materials [97].

The variation of reflection loss (RL) as a function of frequency for experimental/measured thickness of 3 mm, is shown in Fig 14. A reflection loss, or reflectivity, of -10 dB corresponds to 90% of the power incident on the absorber being absorbed or attenuated and is considered the minimum value for an effective EM absorber. It is clear from the plots that reflectivity or reflection loss is minimum in sample $x = 0.8$, with a value of -12.44 dB at 8 GHz and with a -10 dB bandwidth of 1.18 GHz. $x = 0.0$ has RL around -11.83 dB at 8 GHz, and a -10 dB bandwidth of 1.13 GHz.

An interesting point to note is that a useful RL minima is not seen in sample $x = 0.4$, which has a minimum RL of only -4.3 dB, along with the highest dielectric loss and magnetic loss. Poor input impedance matching is the reason for this abnormal behavior. According to this criterion, equality between characteristic impedance and absorber impedance allows the majority of the microwave signal to enter the absorber. On the contrary, the amount of reflected microwave signal from the absorber depends upon the extent of impedance mismatch between the absorber and characteristic impedance. An ideal matching condition has the real impedance $Z_r = Z_o$ (Z_o is the characteristic impedance of free space), and imaginary impedance $Z_{im}=0$. The detailed analysis of this mechanism has been discussed elsewhere [98].

To elucidate this, Fig.14 displays plots of real (Z_r) and imaginary impedance (Z_{im}) associated with the reflection loss for $x = 0.0, 0.4$, and 0.8 compositions. It is evident that for $x = 0.4$, Z_r and Z_{im} are quite far from $Z_o = 377\Omega$ and zero ohm, respectively, with values of 92Ω and -32Ω at 8 GHz. Therefore, the majority of the microwave signal is reflected back

due to the impedance mismatch, and only a small portion of the signal can enter into the absorber, thereby causing lower absorption or small RL in $x = 0.4$. The same mechanism of impedance mismatch is found in samples $x = 1.2, 1.6$ and 2.0 . However, for samples $x = 0.0$ and 0.8 , which had useful reflection loss values at around 8 GHz, Z_r was much higher at 225Ω and 230Ω , respectively, and Z_{im} was smaller, at -23Ω and -11Ω , respectively. Therefore, these had much better impedance matching, and more of the signal was able to enter the sample and be absorbed or attenuated.

Fig.15 represents plots of RL with frequency for measured thickness (t^m) of 3 mm and calculated matching thickness (t^c) derived from quarter wavelength mechanism[98]: this mechanism is associated with maximum absorption for that thickness of composition which is proportional to multiple of quarter wavelength ($\lambda/4$) of the microwave signal.

The calculated thickness is 2.85 mm (8.01 GHz), 1.73 mm (8.0 GHz) and 2.77 mm (8.01) in samples $x = 0.0, 0.4$ and 0.8 , respectively, analogous to the minimum RL of -11.83 dB, -4.3 dB and -12.44 dB, respectively, at 3 mm measured thickness. Thus, t_c is more near to t_m in $x = 0.0$ and 0.8 than $x = 0.4$, which is also the attributing factor to the large absorption or low reflection loss in the same samples. The plots for the rest of the compositions are not displayed as they exhibited a large difference between t_c and t_m . Porosity also can play an important role for the attenuation of the microwave signal from multiple reflections inside the material. Sample $x = 0.8$ has the highest porosity of 31.56%, and it also features the maximum reflection loss among the samples.

The nature of a hard ferrite discourages microwave absorption [100], since hard ferrites have a large coercivity and remanent magnetization; thus they are not able to magnetize and demagnetize in accordance with the changing positive and negative cycles of the microwave signal. Therefore, the signal tends to pass through the sample with low absorption. Samples $x = 1.6$ and 2.0 have the largest coercivities, and hence the large hysteresis losses of 95.7 kAm^{-1} (1199.6 Oe) and 183.4 kA m^{-1} (2299.6 Oe) respectively and, therefore, a low RL or microwave absorption is observed in these samples, which also suffered impedance mismatch and the non-existence of quarter wavelength criteria.

4. Conclusions

Ga substituted $\text{Sr}_3\text{Co}_{2-x}\text{Ga}_x\text{Fe}_{24}\text{O}_{41}$ ($x = 0.0, 0.4, 0.8, 1.2, 1.6, 2.0$) Z-type hexaferrites have been prepared by the sol-gel auto combustion process. XRD studies of $x = 0.0, 0.4, 0.8$

and 1.2 samples reveals the formation of a single Z-phase, while $x = 1.6$ and 2.0 shows the Z-phase along with some M-phase. Magnetic analysis of all samples depict a soft magnetic behavior, except for samples $x = 1.6$ and 2.0, which contained some M phase and hence showed hard ferrite characteristics. Mössbauer spectroscopy confirmed the presence of only Fe^{3+} ions below $x \leq 0.4$ compositions. Beyond $x \geq 0.8$ composition, Fe^{2+} ions were also present (0.4 - 1.3%) in the paramagnetic state. At low frequencies, the dielectric constant of the samples decreases with Ga substitution except for $x = 1.2$. The $x = 0.0$ sample and fully substituted sample ($x = 2.0$), both show loss peaks at ~ 1.18 kHz and ~ 13.296 kHz, respectively. The substitution of gallium caused the enhancement of dielectric properties more than magnetic properties over the investigated X-band. More than 90% microwave absorption (over -10 dB) was noted in samples $x = 0.0$ and 0.8 at GHz, attributing to impedance matching, quarter wavelength mechanism and low coercivity, rendering their potential use for microwave absorbers as suppression of electromagnetic interference.

Acknowledgements

This work was supported by DRS-SAP (Phase-II, F-530/17/DRS-II/2018 (SAP-I)) grant of UGC, New Delhi, India and DST-FIST ((level-I, No.SR/FST/PSI-198/2014)) grant, Department of Science and Technology, India. This work was developed within the scope of the project CICECO-Aveiro Institute of Materials, UIDB/50011/2020 & UIDP/50011/2020, financed by national funds through the FCT/MEC and when appropriate co-financed by FEDER under the PT2020 Partnership Agreement, and R.C. Pullar thanks FCT (Fundação para a Ciência e a Tecnologia, Portugal) grant IF/00681/2015 for supporting this work.

References

- [1]. J. Singh, C. Singh, D. Kaur, S. BindraNarang, R. Jotania, R. Joshi, Microwave absorbing characteristics in Co^{2+} and Al^{3+} substituted $\text{Ba}_{0.5}\text{Sr}_{0.5}\text{Co}_x\text{Al}_x\text{Fe}_{12-2x}\text{O}_{19}$ hexagonal ferrite. *J. Mater. Sci. J. Mater. Sci.: Mater. Electron.* 28 (2017) 2377–2384.
- [2]. A. Sharbati, G. R. Amiri, Magnetic, microwave absorption and structural properties of Mg–Ti added Ca–M hexaferrite nanoparticles. *J. Mater. Sci. Mater. Electron.* 29 (2018) 1118–1122.
- [3]. X. Chen, X Wang, L. Li and S. Qi, Preparation and excellent microwave absorption properties of silver/strontium ferrite/graphite nanosheet composites via sol-gel method, *J. Mater. Sci. Mater. Electron.* 27 (2016) 10045–51.
- [4]. R. C. Pullar, S. G. Appleton, A. K. Bhattacharya, The microwave properties of aligned hexagonal ferrite fibers, *J. Mater. Sci. Lett.* 17(1998) 973-975.

- [5]. J. Smit and H. P. J. Wijn, in "Ferrites", Philips Technical Library, Eindhoven, (1959).
- [6]. M.A. Vinnik, Phase relationships in the BaO-CoO-Fe O system, Russ. J. Inorg. Chem. 10 (1965) 1164-1167.
- [7]. R.C. Pullar, Hexagonal ferrites: a review of the synthesis, properties and applications of hexaferrite ceramics, Prog. Mater. Sci. 57 (2012) 1191–1334.
- [8]. I. Gordon, R.L. Harvey, R.A. Braden, Preparation and magnetic properties of some hexagonal magnetic oxides, J. Am. Ceram. Soc. 45 (1962) 297–301.
- [9]. R. C. Pullar, S. G. Appleton, M. H. Stacey, M. D. Taylor, A. K. Bhattacharya, The synthesis and characterisation of aligned fibres of the ferroxplana ferrites Co_2Z , 0.67% CaO-doped Co_2Z , Co_2Y and Co_2W , J. Magn. Mag. Mater 186 (1998) 313-325.
- [10]. H. Zhang, X. Yao, M. Wu, L. Zhang, Complex permittivity and permeability of Zn-Co substituted Z type hexaferrite prepared by citrate sol-gel process, Br. Ceram. Trans. 102 (2003) 10–15.
- [11]. X. Wang, L. Li, S. Su, Z. Gui, Z. Yue, J. Zhou, Low-temperature sintering and high frequency properties of Cu-modified Co_2Z hexaferrite, J. Eur. Ceram. Soc. 23 (2003) 715–720.
- [12]. X. Wang, L. Li, S. Su, Z. Yue, Electromagnetic properties of low-temperature-sintered $\text{Ba}_3\text{Co}_{2-x}\text{Zn}_x\text{Fe}_{24}\text{O}_{41}$ ferrites prepared by solid state reaction method, J. Magn. Magn. Mater. 280 (2004) 10–13.
- [13]. Z. Li, L. Chen, C. Ong, Z. Yang, Static and dynamic magnetic properties of Co_2Z barium ferrite nanoparticle composites, J. Mater. Sci. 40 (2005) 719–723.
- [14]. Z. W. Li, Z. H. Yang, L. B. Kong, Enhanced microwave magnetic and attenuation properties for Z-type barium ferrite composites with flaky fillers, J Appl Phys. 110 (2011) 063907 (1-7).
- [15]. Z. W. Li, L. Guoqing, L. Chen, W. Yuping, C. K. Ong, Co^{2+} Ti^{4+} substituted Z-type barium ferrite with enhanced imaginary permeability and resonance frequency. J Appl Phys. 99 (2006) 063905 (1-7).
- [16]. J. Xu, C. M. Yang, H. F. Zou, Y. H. Song, G. M. Gao, B. C. An, S. Gan, Electromagnetic and microwave absorbing properties of Co_2Z -type hexaferrites doped with La^{3+} . J. Magn. Magn. Mater. 321 (2009) 3231–3235.
- [17]. S. Zhou, Y. Chen, X. M. Qin. Microwave absorbing properties of Z-type hexaferrite $\text{Ba}_3(\text{MnZn})_x\text{Co}_{2(1-x)}\text{Fe}_{24}\text{O}_{41}$, J Funct Mater. 42 (2011) 1810–1813.
- [18]. Z. Li, Y. Wu, G. Lin, L. Chen, Static and dynamic magnetic properties of CoZn substituted Z-type barium ferrite $\text{Ba}_3\text{Co}_x\text{Zn}_{2-x}\text{Fe}_{24}\text{O}_{41}$ composites, J. Magn. Magn. Mater. 310 (2007) 145–151.
- [19]. R. C. Pullar, A.K. Bhattacharya, The synthesis and characterization of the hexagonal Z ferrite, $\text{Sr}_3\text{Co}_2\text{Fe}_{24}\text{O}_{41}$, from a sol-gel precursor, Mater. Res. Bull. 36 (2001) 1531–1538.
- [20]. T. Kikuchi, T. Nakamura, T. Yamasaki, M. Nakanishi, T. Fujii, J. Takada, Y. Ikeda, Synthesis of single-phase $\text{Sr}_3\text{Co}_2\text{Fe}_{24}\text{O}_{41}$ Z-type ferrite by polymerizable complex method, Mater. Res. Bull. 46 (2011) 1085–1087.

- [21]. H. Zhang, L. Li, J. Zhou, Z. Yue, Z. Ma, Z. Gui, Microstructure characterization and properties of chemically synthesized Co_2Z hexaferrite, *J. Euro. Ceram. Soc.* 21 (2001) 149-153.
- [22]. P. Azizi, S. M. Masoudpanah, S. Alamolhoda, Magnetic and microwave absorption properties of $\text{SrZnCoFe}_{16}\text{O}_{27}$ powders synthesized by solution combustion method, *J. Alloys Comp.* 739 (2018) 211-217.
- [23]. S. Sharma, K. Daya, S. Sharma, K.M. Batoo, M. Singh, Sol-gel auto combustion processed soft Z-type hexanano ferrites for microwave antenna miniaturization, *Ceram. Int.* 41 (2015) 7109-7114.
- [24]. P. Daigle, M. Geiler, A. Geiler, E. DuPre, J. Modest, Y. Chen, C. Vittoria, V. G. Harris, Permeability spectra of Co_2Z hexaferrite compacts produced via a modified aqueous co-precipitation technique, *J. Magn. Magn Mater.* 324 (2012) 3719-3722.
- [25]. K. Seok Moon, Y. M. Kang, I. Han, S. E. Lee, Grain growth behavior of $\text{Ba}_{1.5}\text{Sr}_{1.5}\text{Co}_2\text{Fe}_{24}\text{O}_{41}$ flakes in molten salt synthesis and the magnetic properties of flake/polymer composites, *J. Appl. Phys.* 120 (2016) 194102 (1-9).
- [26]. R. Tang, C. Jiang, H. Zhou, H. Yang, Effects of composition and temperature on the magnetic properties of $(\text{Ba,Sr})_3\text{Co}_2\text{Fe}_{24}\text{O}_{41}$ Z type hexaferrites, *J. Alloy. Compd.* 658 (2016) 132-138.
- [27]. Y. Ye, Q. Liu, J. Wang, Influence of saccharides chelating agent on particle size and magnetic properties of Co_2Z hexaferrite synthesized by sol-gel method, *J. Sol-Gel Sci Technol.* 60 (2011) 41-47.
- [28]. L. Qin, H. Verweij, Modified Pechini synthesis of hexaferrite Co_2Z with high permeability, *Mater. Lett.* 68 (2012) 143-145.
- [29]. L. Jia, H. Zhang, L. Xu, F. Bai, B. Liu, Synthesis and Magnetic Properties of Non-Stoichiometric Co_2Z Hexaferrite, *IEEE Trans. Magn.* 49 (2013) 4281-4283.
- [30]. S. Bae, Y. K. Hong, J. J. Lee, J. Jalli, G. S. Abo, A. Lyle, I. T. Nam, W. M. Seong, J. S. Kum, S. H. Park M, New Synthetic Route of Z-Type ($\text{Ba}_3\text{Co}_2\text{Fe}_{24}\text{O}_{41}$) Hexaferrite Particles, *IEEE Trans. Magn.* 45 (2009) 2557-2560.
- [31]. L. Junliang, Z. Yanwei, G. Cuijing, Z. Wei, Y. Xiaowei, One-Step Synthesis of Barium Hexaferrite Nanocrystals via Microwave-Assisted Sol-Gel Auto-Combustion, *J. Euro. Ceram. Soc.* 30 (2010) 993-997.
- [32]. L. Junliang, Z. Wei, G. Cuijing, Z. Yanwei, Synthesis and Magnetic Properties of Quasi Single Domain M-type Barium Hexaferrite Powders via Sol-Gel Auto-Combustion: Effects of pH and the Ratio of Citric Acid to Metal Ions (CA/M), *J. Alloy. Compd.* 479 (2009) 863-869.
- [33]. S. V. Trukhanov, A. V. Trukhanov, V. G. Kostishyn, L. V. Panina, An. V. Trukhanov, V. A. Turchenko, D. I. Tishkevich, E. L. Trukhanova, O. S. Yakovenko, L. Yu. Matsui, Investigation into the structural features and microwave absorption of doped barium hexaferrites, *Dalton Trans.* 46 (2017) 9010- 9021.
- [34]. S. V. Trukhanov, A. V. Trukhanov, V. G. Kostishin, L. V. Panina, I. S. Kazakevich, V. A. Turchenko, V. V. Oleinik, E. S. Yakovenko and L. Y. Matsui, Magnetic and

- Absorbing Properties of M-type Substituted Hexaferrites $\text{BaFe}_{12-x}\text{Ga}_x\text{O}_{19}$ ($0.1 < x < 1.2$), *J. Exp. Theor. Phys.* 123(2016) 461–469.
- [35]. A. V. Trukhanov, S. V. Trukhanov, V. A. Turchenko, V. V. Oleinik, E. S. Yakovenko, L. Y. Matsui, L. L. Vovchenko, V. L. Launets, I. S. Kazakevich, S. G. Dzhabarov, Crystal Structure, Magnetic, and Microwave Properties of Solid Solutions $\text{BaFe}_{12-x}\text{Ga}_x\text{O}_{19}$ ($0.1 \leq x \leq 1.2$), *Phys. Solid State* 58 (2016) 1792–1797.
- [36]. S. V. Trukhanov, A. V. Trukhanov, V. G. Kostishyn, L. V. Panina, An. V. Trukhanov, V. A. Turchenko, D. I. Tishkevich, E. L. Trukhanova, O. S. Yakovenko, L. Yu. Matzui, D. A. Vinnik and D. V. Karpinsky, Effect of gallium doping on electromagnetic properties of barium hexaferrite, *J. Phys. Chem. Solids*, 111 (2017) 142–152.
- [37]. S. V. Trukhanov, A. V. Trukhanov, V. G. Kostishyn, L. V. Panina, An. V. Trukhanov, V. A. Turchenko, D. I. Tishkevich, E. L. Trukhanova, V. V. Oleynik, O. S. Yakovenko, L. Yu. Matzui and D. A. Vinnik, Magnetic, dielectric and microwave properties of the $\text{BaFe}_{12-x}\text{Ga}_x\text{O}_{19}$ ($x \geq 1.2$) solid solutions at room temperature, *J. Magn. Mag. Mater.* 442 (2017) 300–310.
- [38]. S. V. Trukhanov, A. V. Trukhanov, V. G. Kostishyn, N. S. Zabeivorot, L. V. Panina, An. V. Trukhanov, V. A. Turchenko, E. L. Trukhanova, V. V. Oleynik, O. S. Yakovenko, L. Yu. Matzui and V. E. Zhivulin, High-frequency absorption properties of gallium weakly doped barium hexaferrites, *Philos Mag.* 99 (2019) 585–605.
- [39]. I. Ali, M. U. Islam, M. S. Awan, M. Ahmad, Electric and Dielectric Properties of Cr-Ga Substituted BaM Hexaferrites for High-Frequency Applications, *J. Mater. Eng. Perform.* 22 (2013) 2673–2680.
- [40]. D. Guo, W. Kong, J. Feng, X. Li, X. Fan, Microwave absorption properties of $\text{Sr}_x\text{Ba}_{3-x}\text{Co}_2\text{Fe}_{24}\text{O}_{41}$ hexaferrites in the range of 0.1–18 GHz, *J. Alloy Compd.* 751 (2018) 80–85
- [41]. S. Kumar, D. P. Dubey, S. Shannigrahi, R. Chatterjee, Complex permittivity, permeability, magnetic and microwave absorbing properties of Ni^{2+} substituted mechanically milled U-type hexaferrites, *J. Alloy. Compd.* 774 (2019), 52–60
- [42]. Z. W. Li, Lin Guoqing, Nai-Li Di, Zhao-Hua Cheng, C. K. Ong, Mössbauer spectra of CoZn-substituted Z-type barium ferrite $\text{Ba}_3\text{Co}_{2-x}\text{Zn}_x\text{Fe}_{24}\text{O}_{41}$. *Phys. Rev. B.* 72, (2005) 104420 (1–7).
- [43]. A. R. Kagdi, N. P. Solanki, F. E. Carvalho, S. S. Meena, P. Bhatt, R. C. Pullar, R. B. Jotania, Influence of Mg substitution on structural, magnetic and dielectric properties of X-type barium-zinc hexaferrites $\text{Ba}_2\text{Zn}_{2-x}\text{Mg}_x\text{Fe}_{28}\text{O}_{46}$, *J. Alloy. Compd.* 741 (2018) 377–391.
- [44]. F. M. M. Pereria, C. A. R. Junior, M. R. P. Santosh, R. S. T. M. Sohn, F. N. A. Freire, J. M. Sasaki, J. A. C. De-Paiva, A. B. S. Sombra, Structural and dielectric spectroscopic studies of M-type barium hexaferrite alloys ($\text{Ba}_x\text{Sr}_{1-x}\text{Fe}_{12}\text{O}_{19}$), *J. Mater. Sci. Mater. Electron.* 19 (2008) 627–638.
- [45]. M. Ghobeiti Hasab, S. A. Seyyed Ebrahimi, A. Badiei, M. Ghobeiti Hasab, S. A. Seyyed Ebrahimi, A. Badiei, Effect of different fuels on the strontium hexaferrite nanopowder synthesized by a surfactant-assisted sol–gel auto-combustion method, *J. Non-Cryst. Solids* 353 (2007) 814–816.

- [46]. S.M. El-Sayed, T.M. Meaz, M.A. Amer, H.A. El Shersaby, Magnetic behavior and dielectric properties of aluminum substituted M-type barium hexaferrite, *Physica B*. 426 (2013) 137–143.
- [47]. R. D. Shannon, Revised Effective Ionic Radii and Systematic Studies of Interatomic Distances in Halides and Chalcogenides, *Acta Cryst. A*32 (1976) 751-767.
- [48]. H. Kojima, in: E.P. Wohlfarth (Ed.), *Ferromagnetic Materials*, vol. 3, North Holland, Amsterdam, 1982, p. 305.
- [49]. M.J. Iqbal, S. Farooq, Could binary mixture of Nd–Ni ions control the electrical behavior of strontium–barium M-type hexaferrite nanoparticles, *Mater. Res. Bull.* 46 (2011) 662-667.
- [50]. A. Thakur, R.R. Singh, P.B. Barman, Synthesis and characterizations of Nd³⁺ doped SrFe₁₂O₁₉ nanoparticles, *Mater. Chem. Phys.* 141 (2013) 562-569.
- [51]. R. L. Coble and J. E. Burke, *Sintering in Ceramics*, Progress in Ceramic Science, Pergamon Press, New York, 1964.
- [52]. S. Ashima, S. Sanghia, A. Agarwal, Reetu, N. Ahlawat, Monica, Structure refinement and dielectric relaxation of M-type Ba, Sr, Ba-Sr, and Ba-Pb hexaferrites, *J. Appl. Phys.* 112, (2012) 014110 (1-7).
- [53]. V.R.K. Murthy, J. Sobhanadri, Dielectric properties of some nickel-zinc ferrites at radio frequency, *Phys. Stat. Sol. A* 36 (1976) K133-K135.
- [54]. A. Gonchar, S. Gorelik, S. Katynkina, L. Letyuk, I. Ryabov, The regularity of microstructure formation and its influence on the properties of soft magnetic ferrites, *J. Magn. Magn. Mater.* 215–216 (2000) 221–223.
- [55]. M. Hashim, Alimuddin, S. Kumar, S. E. Shirsath, E. M. Mohammed, R. Kumar, Structural, Dielectric, AC Conductivity, and Magnetic Properties of Cr³⁺ Substituted Ni–Mg Ferrite Nanoparticles, *J. Nanoeng. Nanomanuf.* 3 (2013) 1–8.
- [56]. R. C. Pullar, P. Marques, J. Amaral, J. A. Labrincha, Magnetic wood-based biomorphic Sr₃Co₂Fe₂₄O₄₁ Z-type hexaferrite ecoceramics made from cork templates, *Mater. Des.* 82 (2015) 297–303.
- [57]. Y. Kitagawa, Y. Hiraoka, T. Honda, T. Ishikura, H. Nakamura, T. Kimura, Low-field magnetoelectric effect at room temperature, *Nat. Mater.* 9 (2010) 797–802.
- [58]. Y. Takada, T. Nakagawa, M. Tokunaga, Y. Fukuta, T. Tanaka, T.A. Yamamoto, T. Tachibana, S. Kawano, Y. Ishii, N. Igawa, Crystal and magnetic structures and their temperature dependence of Co₂Z-type hexaferrite (Ba,Sr)₃Co₂Fe₂₄O₄₁ by high-temperature neutron diffraction, *J. Appl. Phys.* 100 (2006), 043904.
- [59]. J. Singh, C. Singh, D. Kaur, H. Zaki, I. A Abdel-Latif, S. Bindra Narang, R. Jotania, S. Mishra, R. Joshi, P. Dhruv, M. Ghimire, S. E. Shirsath, S. S. Meena, Elucidation of phase evolution, microstructural, Mössbauer and magnetic properties of Co²⁺-Al³⁺ doped M-type Ba-Sr hexaferrites synthesized by a ceramic method, *J. Alloy. Compd.* 695 (2017) 1112-1121.
- [60]. G. M. Suarez, L.P. Rivas-Vazquez, J. C. Corral-Huacuz, A. F. Fuentes, J. I. Escalante-Garcia, Magnetic properties and microstructure of BaFe_{11.6-2x}Ti_xM_xO₁₉. (M= Co, Zn, Sn) compounds, *Phys. B*, 339 (2003) 110- 118.
- [61]. C. C. Chauhan, A. R. Kagdi, R. B. Jotania, A. Upadhyay, C. Singh Sandhu, S. E. Shirsath, S. S. Meena, Structural magnetic and dielectric properties of Co-Zr substituted

- M-type calcium hexagonal ferrite nanoparticles in the presence of α - Fe_2O_3 phase, *Ceram. Int.* 44 (2018) 17812–17823.
- [62]. V.G. Bhide, Mössbauer Effect and its Applications. Tata McGraw-Hill, New Delhi (1973).
- [63]. U. Ganser, (ed.): Mössbauer Spectroscopy. Springer, New York (1975).
- [64]. J. T. Lim, I. Shim, E. Hahn, C. S. Kim, The crystalline and magnetic properties of Zn doped strontium Z-type hexaferrite synthesized by polymerizable complex method, *AIP ADV.* 7(2017) 056108 (1-6).
- [65]. K. Sharma, S.S. Meena, S. Saxena, S.M. Yusuf, A. Srinivasan, G.P. Kothiyal, Structural and magnetic properties of glass-ceramics containing silver and iron oxide, *Mater. Chem. Phys.* 133 (2012) 144-150.
- [66]. K. Sharma, A. Dixit, Sher Singh, Jagannath, S. Bhattacharya, C.L. Prajapat, P.K. Sharma, S.M. Yusuf, A.K. Tyagi, G.P. Kothiyal, Preparation and studies on surface modifications of calcium-silico-phosphate ferrimagnetic glass-ceramics in simulated body fluid, *Mater. Sci. Eng. C.* 29 (2009) 2226–2233.
- [67]. K. Sharma, Sher Singh, C.L.Prajapat, S.Bhattacharya, Jagannath, M.R.Singh, S.M. Yusuf, G.P. Kothiyal, Preparation and study of magnetic properties of silico phosphate glass and glass-ceramics having iron and zinc oxide, *J Magn Magn Mater.* 321 (2009) 3821–3828.
- [68]. K. Sharma, C.L. Prajapat, S. S. Meena, M.R. Singh, S.M. Yusuf, L. Montagne, G.P.Kothiyal, Influence of Au addition on magnetic properties of iron oxide in a silica-phosphate glass matrix, *J Magn Magn Mater.* 345 (2013)24–28.
- [69]. S.S. Shinde, Sher Singh Meena, S. M. Yusuf, and K. Y. Rajpure, Mössbauer, Raman, and Magnetoresistance Study of Aluminum-Based Iron Oxide Thin Films, *J. Phys. Chem. C.* 115 (2011) 3731–3736.
- [70]. S. Katlakunta, S.S. Meena, S. Srinath, M. Bououdina, R. Sandhya, K. Praveena, Improved magnetic properties of Cr^{3+} doped $\text{SrFe}_{12}\text{O}_{19}$ synthesized via microwave hydrothermal route, *Mater. Res. Bull.* 63 (2015) 58-66.
- [71]. V.A. Rane, S.S. Meena, S.P. Gokhale, S.M. Yusuf, G.J. Phatak, S.K. Date, Synthesis of Low Coercive $\text{BaFe}_{12}\text{O}_{19}$ Hexaferrite for Microwave Applications in Low-Temperature Cofired Ceramic, *J. Electronic Materials*, 42 (2013) 761-768.
- [72]. A Mitra, J Mohapatra, S S Meena, CV Tomy, M Aslam, Verwey transition in ultrasmall-sized octahedral Fe_3O_4 nanoparticles, *The Journal of Physical Chemistry C* 118 (33) (2014) 19356-19362.
- [73]. A. Mitra, B. Barick, J. Mohapatra, H Sharma, S. S. Meena, M. Aslam, Large tunneling magnetoresistance in octahedral Fe_3O_4 nanoparticles, *AIP Advances* 6 (5), (201) 055007.
- [74]. A. Mitra, J. Mohapatra, H. Sharma, S. S. Meena, M. Aslam, Controlled Synthesis and Enhanced Tunneling Magnetoresistance in Oriented Fe_3O_4 Nanorod Assemblies, *J.Phys. D: Appl. Phys.* 51 (2018) 085002.
- [75]. R. A. Nandotaria, R. B. Jotania, C. Singh Sandhu, M. Hashim, S.S. Meena, P. Bhatt, S.E. Shirsath, Magnetic interactions and dielectric dispersion in Mg substituted M-

- type Sr-Cu hexaferrite nanoparticles prepared using one step solvent free synthesis technique, *Ceram. Int.* 44 (2018) 4426–4435.
- [76]. G. Aravind, M. Raghasudha, D. Ravinder, M. Manivel Raja, S.S. Meena, Pramod Bhatt, Mohd. Hashim, Study of structural and magnetic properties of Li–Ni nanoferrites synthesized by citrate-gel auto combustion method, *Ceram. Int.* 42 (2016) 2941-2950.
- [77]. Greenwood, N. N.; Gibb, T. C. *Mössbauer Spectroscopy*; Chapman and Hall Ltd.: London, 1971.
- [78]. T. Kikuchi, M. Kobune, M. Nakanishi, T. Fuji, Mössbauer study of zinc-substituted strontium cobalt Z-type hexaferrite, *Ceram. Int.* 43 (2017) S386-S390.
- [79]. P. N. Dhruv, S. S. Meena, R. C. Pullar, F. E. Carvalho, R. B. Jotania, P. Bhatt, C. L. Prajapat, J. P. B. Machado, T. V. C Rao, C. B. Basak, Investigation of structural, magnetic and dielectric properties of gallium substituted Z-type $\text{Sr}_3\text{Ga}_x\text{Co}_{2-x}\text{Fe}_{24}\text{O}_{41}$ hexaferrites for microwave absorbers, *J Alloy Compd.* 822 (20120) 153470 (1-22).
- [80]. C. G. Koops, On the Dispersion of Resistivity and Dielectric Constant of Some Semiconductors at Audio frequencies *Phys. Rev.* 83 (1951) 121-124.
- [81]. P. Vinayak, P. Khirade, S. D. Birajdar, R. C. Alange, K. M. Jadhav, Electrical and Dielectrical Properties of Low-Temperature-Synthesized Nanocrystalline Mg^{2+} Substituted Cobalt Spinel Ferrite, *J Supercond Nov Magn.* 28 (2015) 3351–3356.
- [82]. Ali, M. U. Islam, M.S. Awan, M. Ahmad, Effects of Heat-Treatment Time on the Structural, Dielectric, Electrical, and Magnetic Properties of BaM Hexaferrite, *J. Mater. Eng. Perform.* 22 (2013) 2104-2114.
- [83]. M. N. Ashiq, M. J. Iqbal, I.H. Gul, Effect of Al–Cr doping on the structural, magnetic and dielectric properties of strontium hexaferrite nanomaterials, *J. Magn. Magn. Mater.* 323, (2011) 259-263.
- [84]. S. Ashima, S. Sanghia, A. Agarwal, Reetu, N. Ahlawat, Monica, Structure refinement and dielectric relaxation of M-type Ba, Sr, Ba-Sr, and Ba-Pb hexaferrites, *J. Appl. Phys.* 112, (2012) 014110 (1-7).
- [85]. V.R.K. Murthy, J. Sobhanadri, Dielectric properties of some nickel-zinc ferrites at radio frequency, *Phys. Stat. Sol. A* 36 (1976) K133-K135.
- [86]. M. Hashim, Alimuddin, S. Kumar, S. E. Shirsath, E. M. Mohammed, R. Kumar, Structural, Dielectric, AC Conductivity, and Magnetic Properties of Cr^{3+} Substituted Ni–Mg Ferrite Nanoparticles, *J. Nanoeng. Nanomanuf.* 3 (2013) 1–8.
- [87]. B. Behera, P. Nayak, R. N. P. Choudhary, Impedance spectroscopy study of $\text{NaBa}_2\text{V}_5\text{O}_{15}$ ceramic, *J. Alloys. Compds.* 436 (2007) 226- 232.
- [88]. A. Kumar, B. P. Singh, R.N.P. Choudhary, A. K. Thakur, Characterization of electrical properties of Pb-modified BaSnO_3 using impedance spectroscopy, *Mater. Chem. Phys.*, 99 (2006) 150- 159.
- [89]. A. Gonchar, S. Gorelik, S. Katynkina, L. Letyuk, I. Ryabov, The regularity of microstructure formation and its influence on the properties of soft magnetic ferrites, *J. Magn. Magn. Mater.* 215–216 (2000) 221–223.

- [90]. K.P. Padmasree, D.K. Kanchan, A.R. Kulkarni, Impedance and modulus studies of the solid electrolyte system $20\text{CdI}2\text{-}80 [\text{xAg}2\text{O-y}(0.7\text{V}_2\text{O}_{5-0.3}\text{B}_2\text{O}_3)]$, where $1 \leq \text{x/ y} \leq 3$, *Solid State Ion.* 177 (2006) 475–482.
- [91]. B.V.R. Chowdari, R.G. Krishnan, AC conductivity analysis of glassy silver iodomolybdate system, *Solid State Ion.*, 23 (1987) 225–233.
- [92]. V. Provenzano, L. P. Boesch, V. Volterra, C. T. Moynihan, P. B. Macedo, Electrical Relaxation in $\text{Na}_2\text{O}_3\text{SiO}_2$ Glass, *J. Am. Ceram. Soc.*, 55 (1972) 492.
- [93]. S. M. Patange, S.E. Shirsath, K.S. Lohar, S.S. Jadhav, N. Kulkarni, K.M. Jadhav, Electrical and switching properties of $\text{NiAl}_x\text{Fe}_{2-x}\text{O}_4$ ferrites synthesized by chemical method, *Phys. B: Condens. Mater.* 406 (2011) 663–668.
- [94]. Y. Bai, J. Zhou, Z. Gui, L. Li, Electrical properties of non-stoichiometric Y-type hexagonal ferrite, *J. Magn. Magn. Mater.* 278 (2004) 208–213.
- [95]. M. G. Chourashiya, J.Y. Patil, S.H. Pawar, L.D. Jadhav, Studies on structural, morphological and electrical properties of $\text{Ce}_{1-x}\text{Gd}_x\text{O}_{2-(x/2)}$, *Mater. Chem. Phys.* 109 (2008) 39–44.
- [96]. E. Handoko, S. Iwan, S. Budi, B. S. Anggoro, A. M. Mangasi, M. Randa, J. Zulkarnain, C. Kurniawan, N. Sofyan, M. Alaydrus, Magnetic and microwave absorbing properties of $\text{BaFe}_{12-2x}\text{Co}_x\text{Zn}_x\text{O}_{19}$ ($x = 0.0; 0.2; 0.4; 0.6$) nanocrystalline, *Mater. Res. Express.* 5(6)(2018).
- [97]. S. JunHai, C. KeYu, L. I. Liang Chao, D. Yan, L. JuanBi, K. WeiQiu, Fabrication of Z-type barium ferrite/silica composites with enhanced microwave absorption. *Sci China Tech Sci.* 57 (2014) 1858-1864.
- [98]. H. Kaur, A. Marwaha, C. Singh, S. B. Narang, R. Jotania, Y. Bai, S. Mishra, D. Singh, S. Sombra, M. Ghimire, P. Dhruv, Tailoring of electromagnetic absorption in substituted hexaferrites from 8.2 GHz to 12.4 GHz, *J. Electron. Mater.* 49 (2020) 1646–1653.
- [99]. H. Kaur, A. Marwaha, C. Singh, S. Bindra N., R. Jotania, S. Jacobo, S. Sombra, S.V. Trukhanov, A.V. Trukhanov, P. Dhruv, Investigation of structural, hysteresis and electromagnetic parameters for microwave absorption application in doped Ba-Sr hexagonal ferrites at X-band, *J Alloy Compd.* 806 (2019) 1220-1229
- [100]. C. Singh, S. B. Narang, R. Jotania, Microwave Absorption in Ceramics: Different Mechanisms and its Optimization, *Eng. Magnetic, Dielectric and Microwave Properties of Ceramics and Alloys Materials Research Forum LLC Materials Research Foundations* 57 (2019) 175-190.

List of Figures

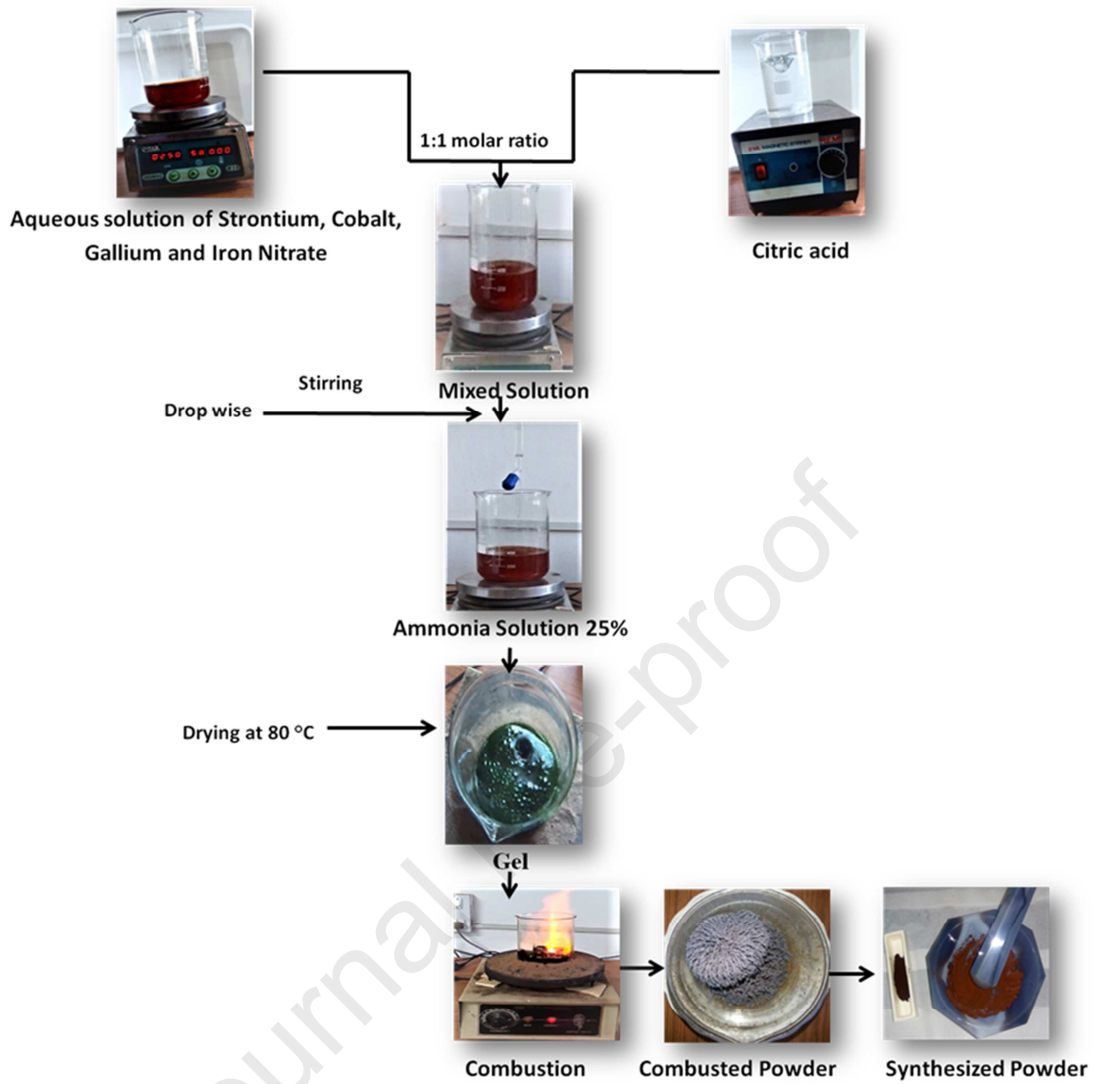


Fig.1. Flowchart for the preparation of Sr₃Ga_xCo_{2-x}Fe₂₄O₄₁ hexaferrite powder samples.

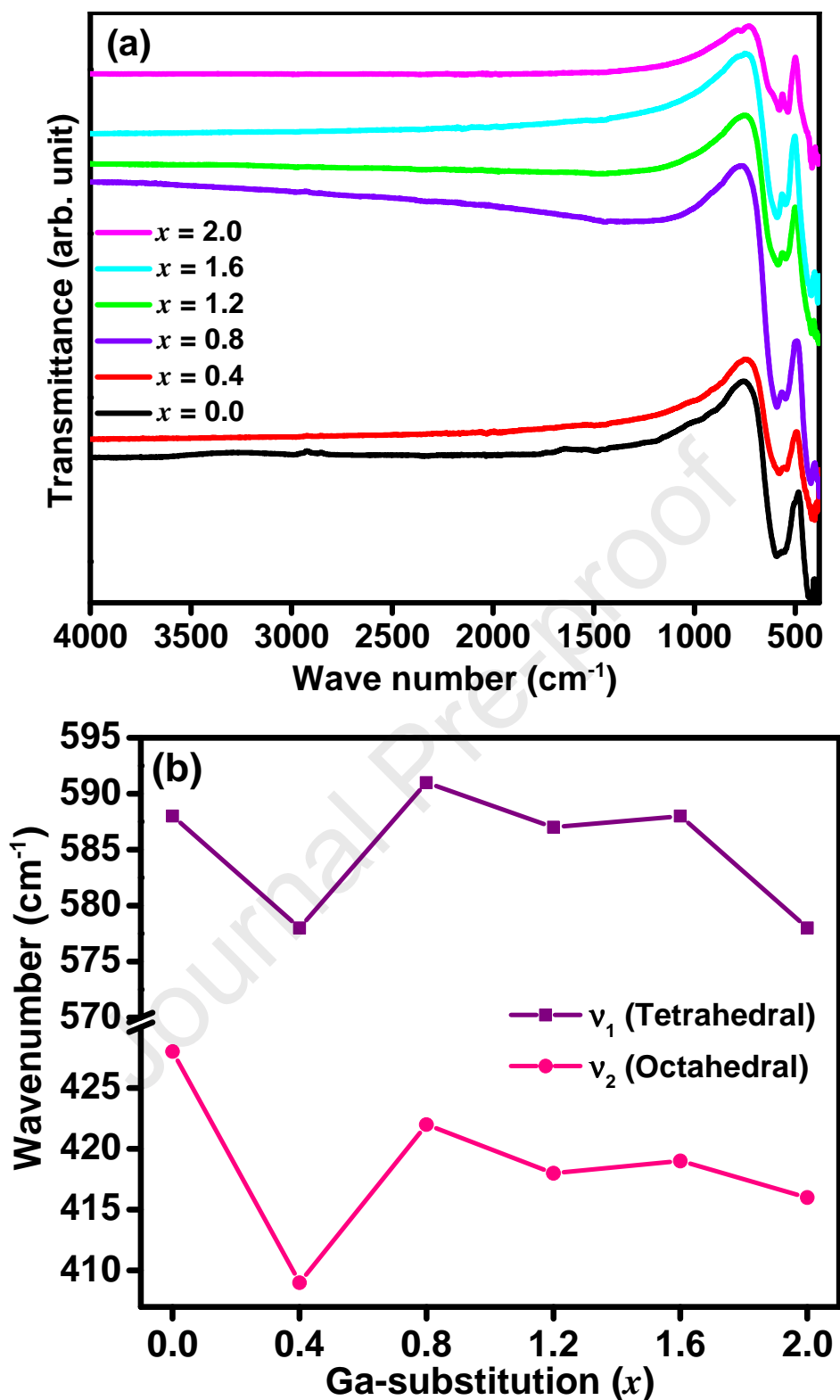
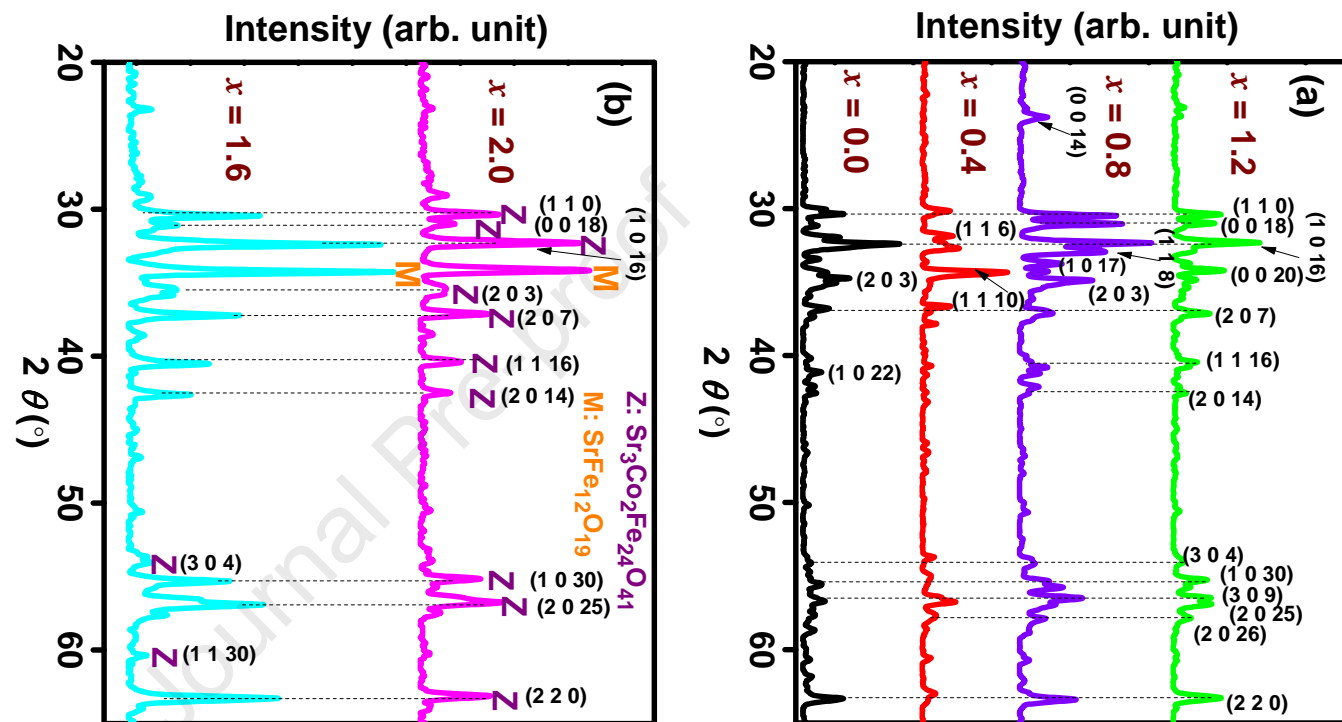


Fig.2 (a). FT-IR spectra of $\text{Sr}_3\text{Ga}_x\text{Co}_{2-x}\text{Fe}_{24}\text{O}_{41}$ powder samples with $x = 0.0, 0.4, 0.8, 1.2, 1.6,$ and 2.0 , heated at $1150\text{ }^\circ\text{C}$ for 5 h , and (b) variation in vibrations with Ga substitution (x) of tetrahedral (ν_1) and octahedral (ν_2) metal-oxygen bonds.



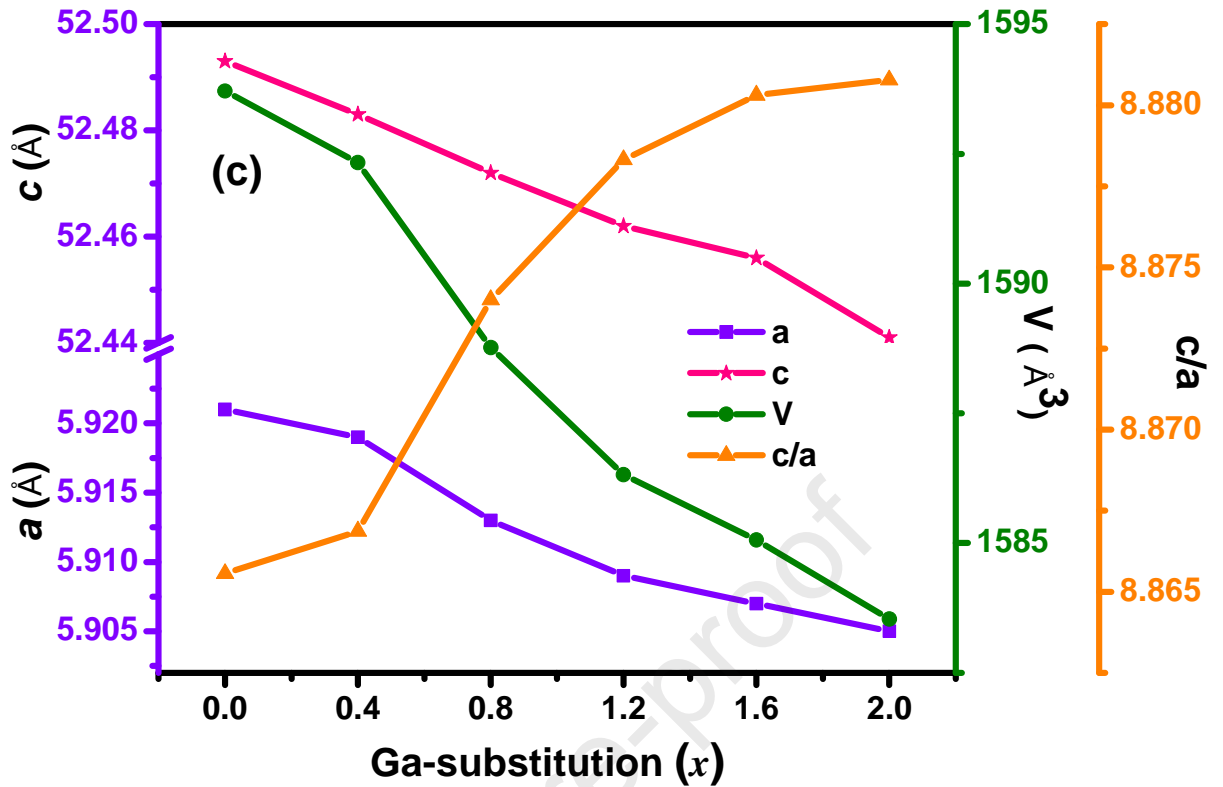


Fig. 3. XRD patterns of $\text{Sr}_3\text{Ga}_x\text{Co}_{2-x}\text{Fe}_{24}\text{O}_{41}$ (a) $x = 0.0, 0.4, 0.8,$ and 1.2 ; (b) $x = 1.6$ and 2.0 hexaferrite powder samples heated at 1150°C for 5 h.; (c) The change in lattice constants (a , c), unit cell volume (V) and variation in the aspect ratio (c/a) versus Ga substitution (x).

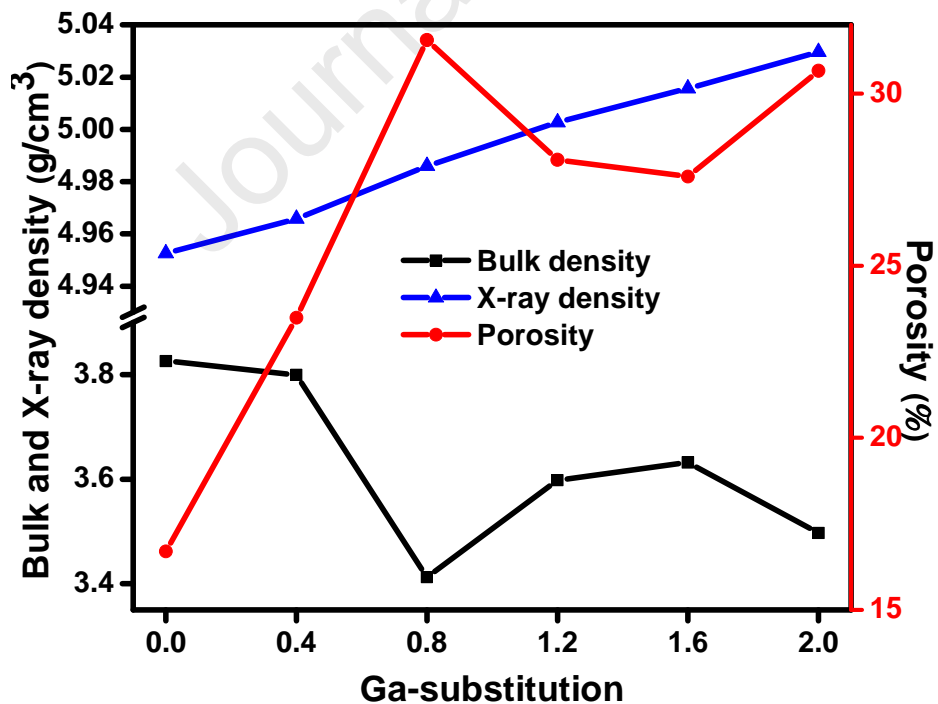


Fig.4. Variation of the Bulk density, X-ray density and Porosity with Ga substitution (x).

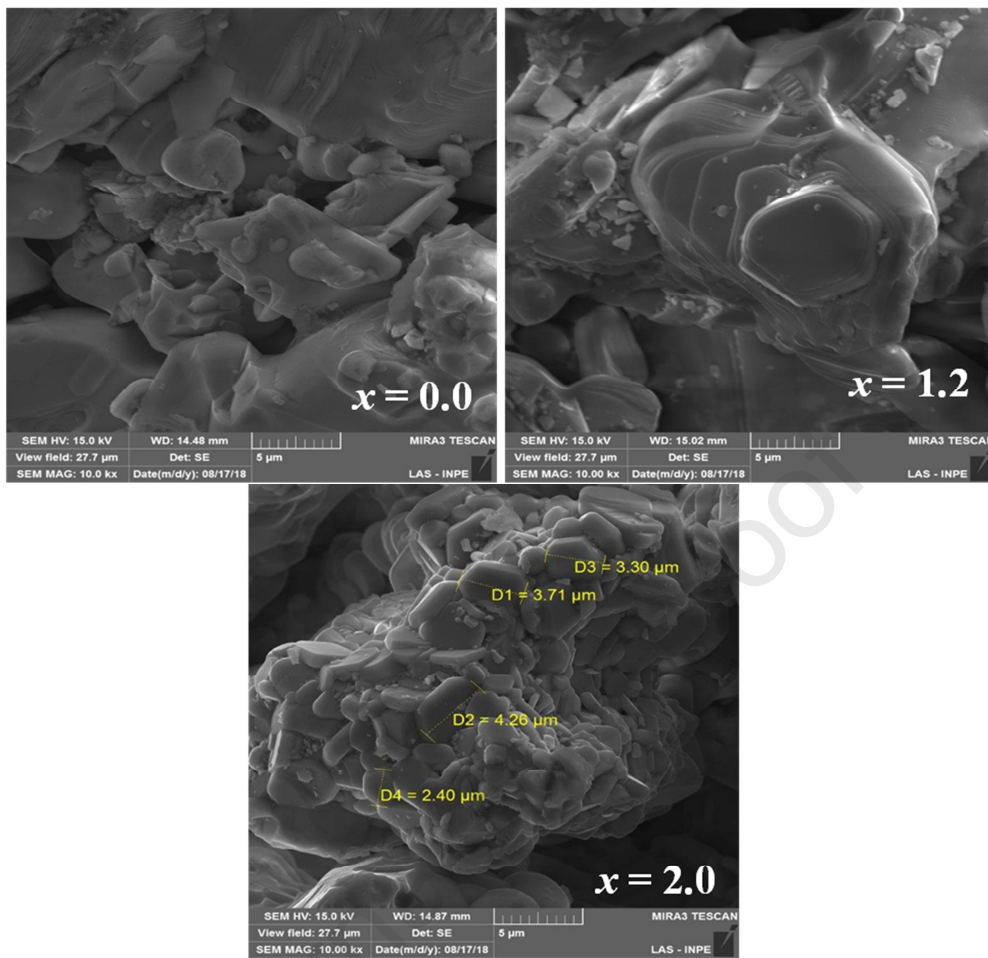
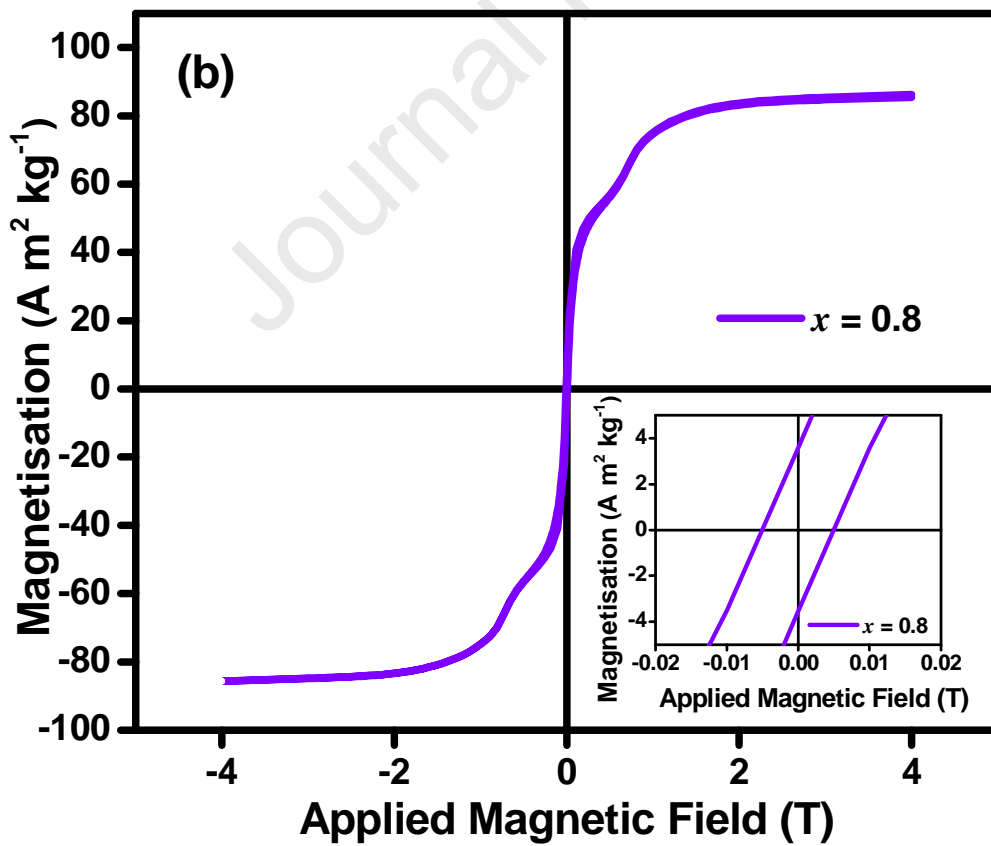
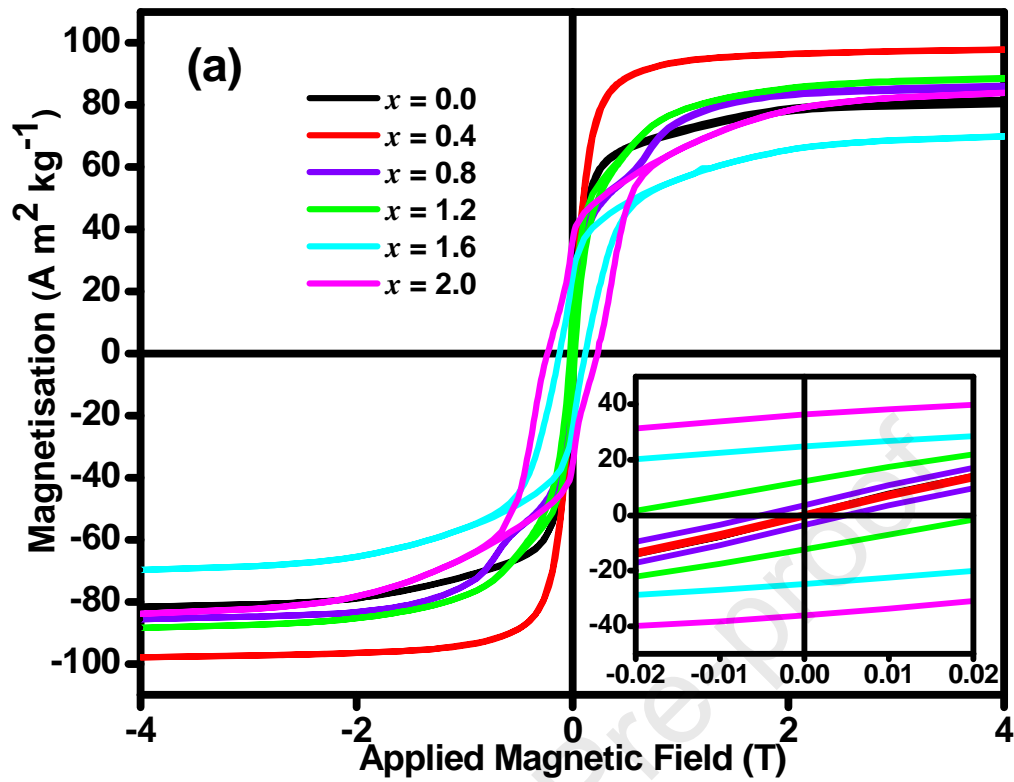


Fig. 5. FE-SEM images of $\text{Sr}_3\text{Ga}_x\text{Co}_{2-x}\text{Fe}_{24}\text{O}_{41}$ ($x = 0.0, 1.2, \text{ and } 2.0$) hexaferrite samples heated at $1150\text{ }^\circ\text{C}$ for 5 h.



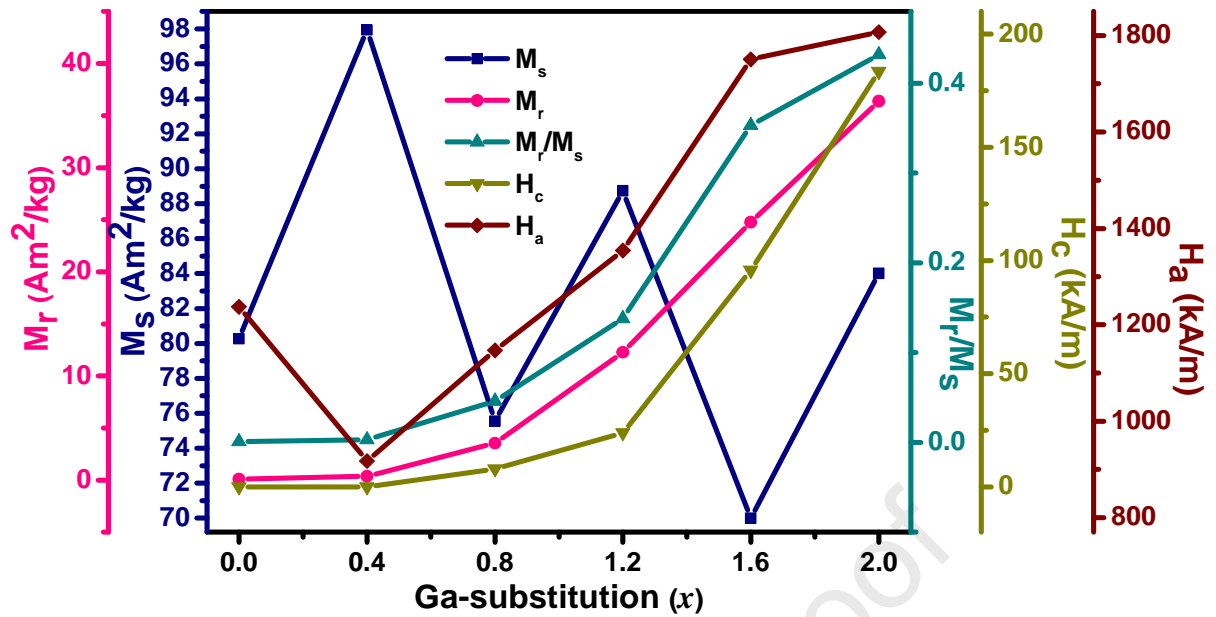


Fig. 6 (a). Room temperature magnetic hysteresis loops of $\text{Sr}_3\text{Ga}_x\text{Co}_{2-x}\text{Fe}_{24}\text{O}_{41}$ ($x = 0.0, 0.4, 0.8, 1.2, 1.6,$ and 2.0) hexaferrite powder samples heated at $1150\text{ }^\circ\text{C}$ for 5 h., (b) the individual hysteresis loop of $\text{Sr}_3\text{Ga}_{0.8}\text{Co}_{1.2}\text{Fe}_{24}\text{O}_{41}$ ($x = 0.8$), (c) Variation of remanent magnetisation (M_r), saturation magnetisation (M_s), coercive field (H_c), squareness ratio (M_r/M_s) and anisotropy field (H_a) with Ga substitution

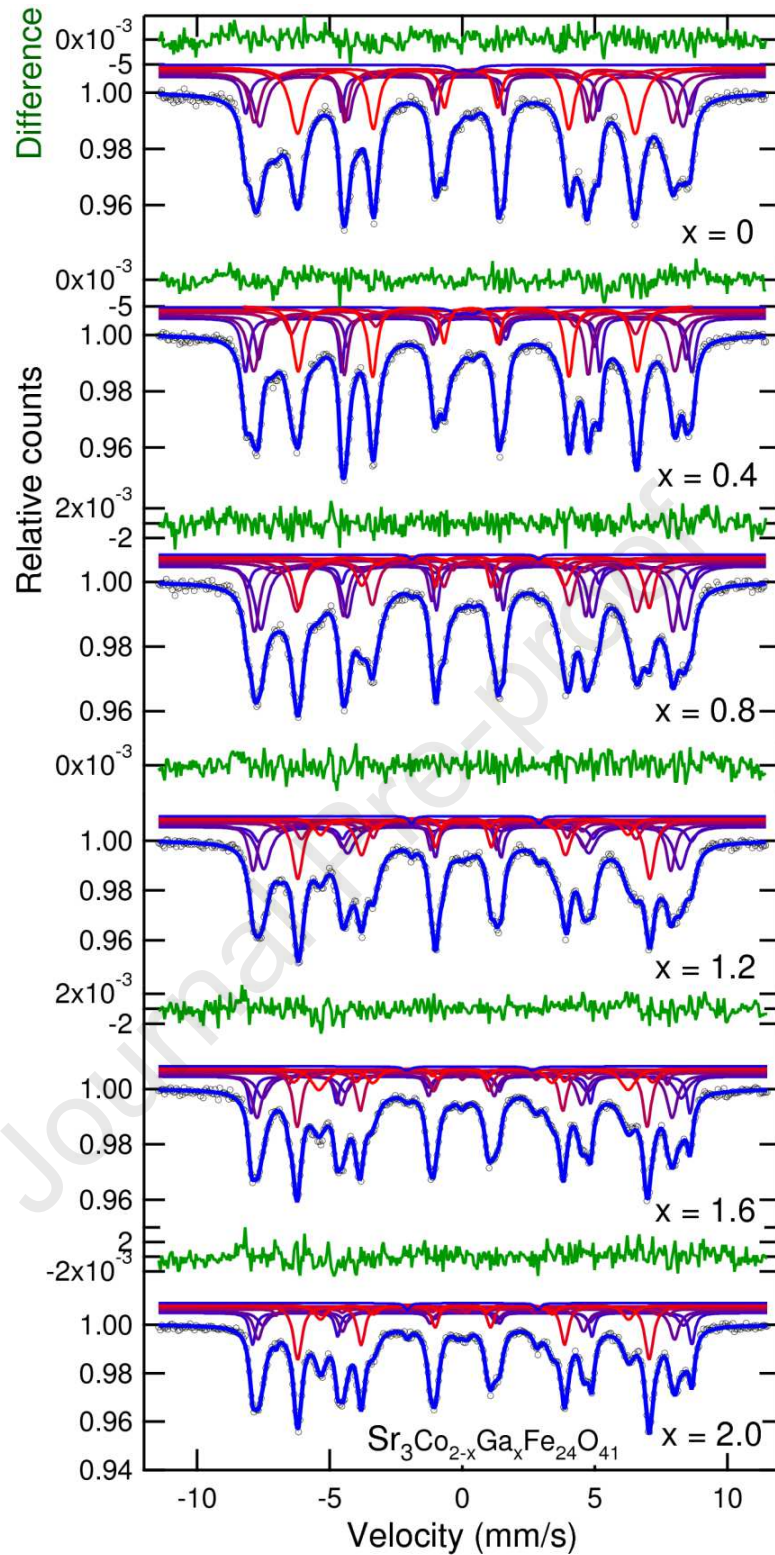
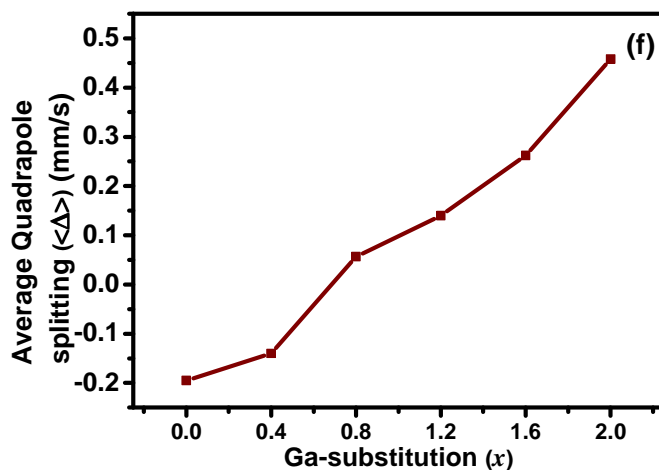
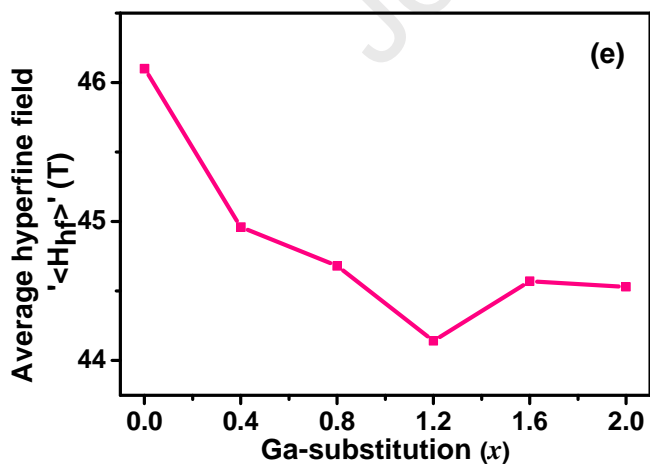
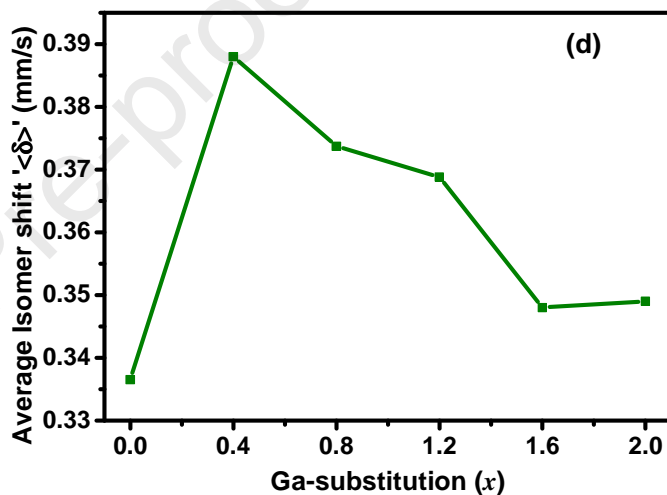
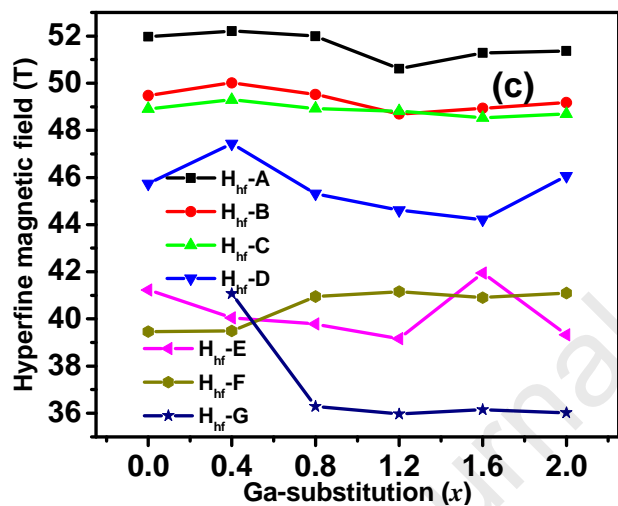
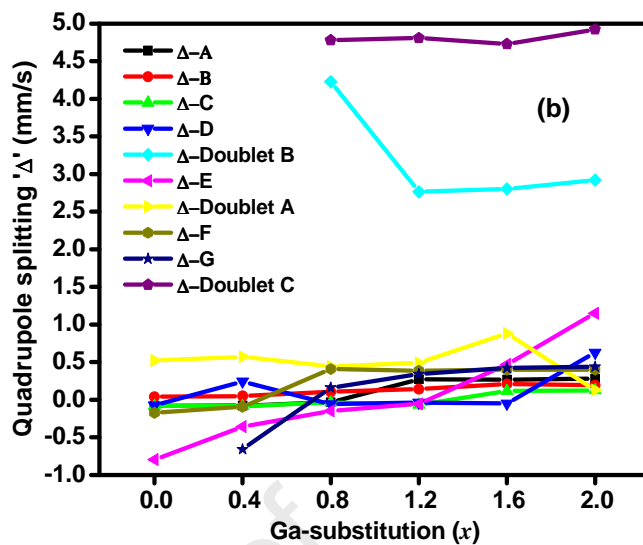
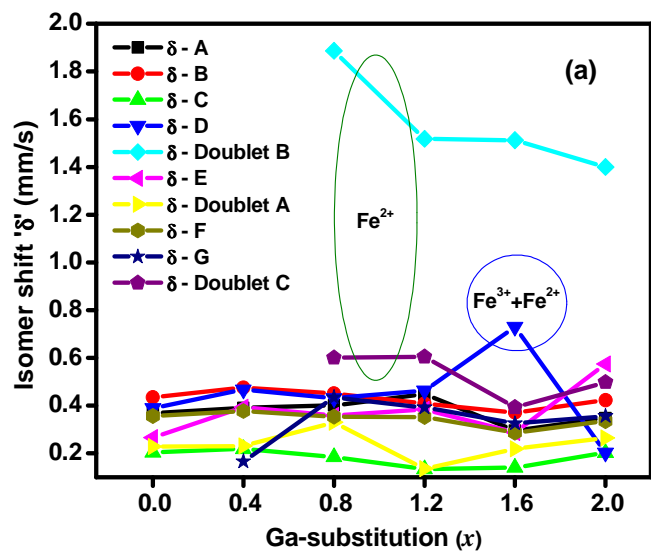


Fig.7. Room temperature Mössbauer spectra of $\text{Sr}_3\text{Co}_{2-x}\text{Ga}_x\text{Fe}_{24}\text{O}_{44}$ ($x = 0.0, 0.4, 0.8, 1.2, 1.6,$ and 2.0) hexaferrite samples heated at $1150\text{ }^\circ\text{C}$ for 5 h.



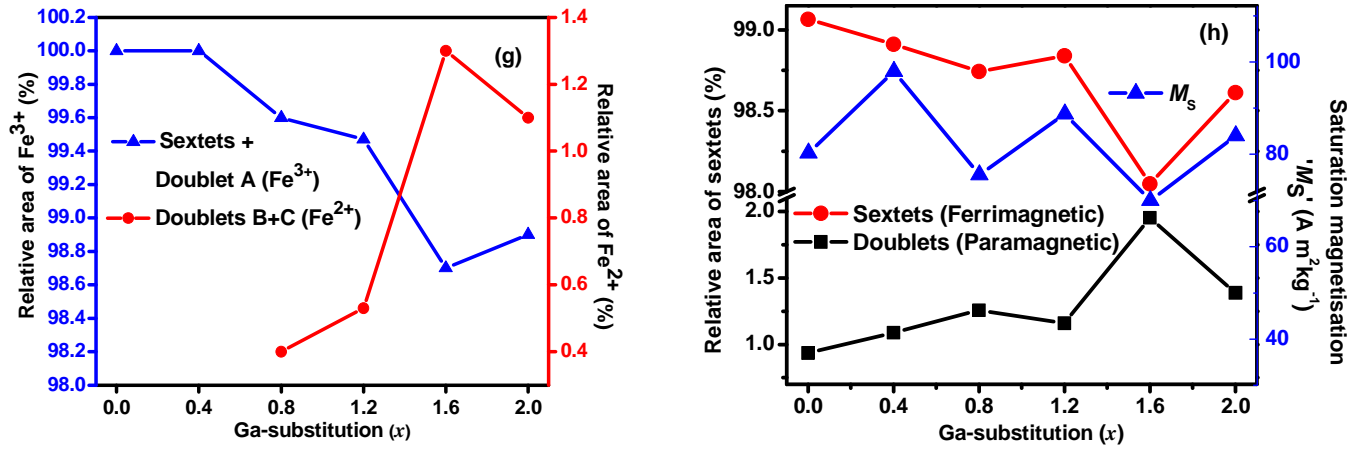
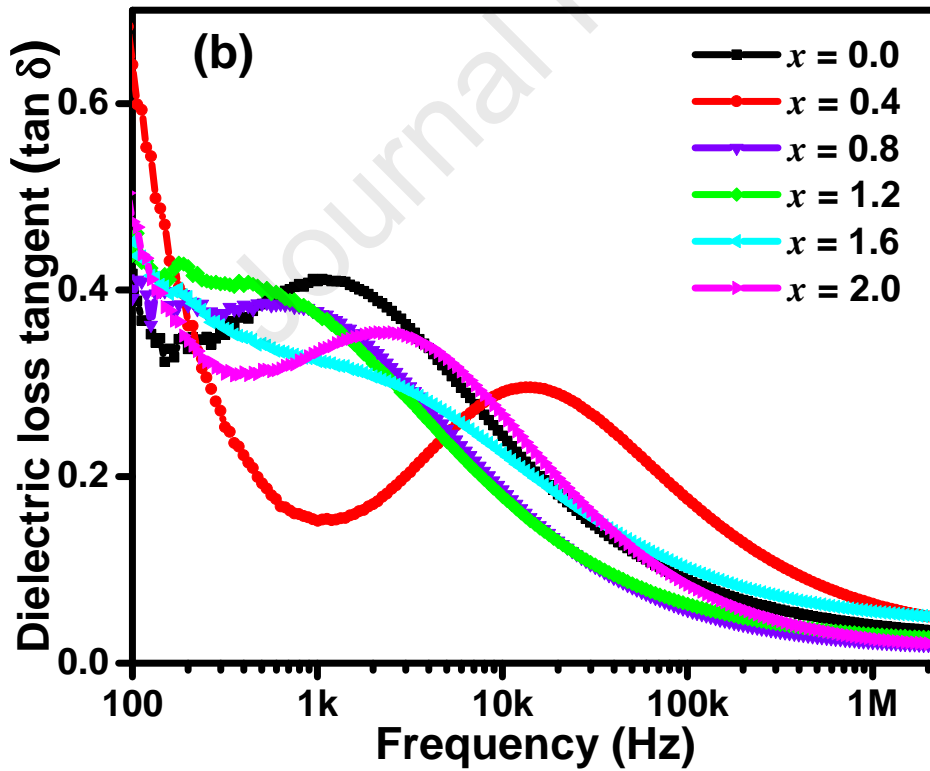
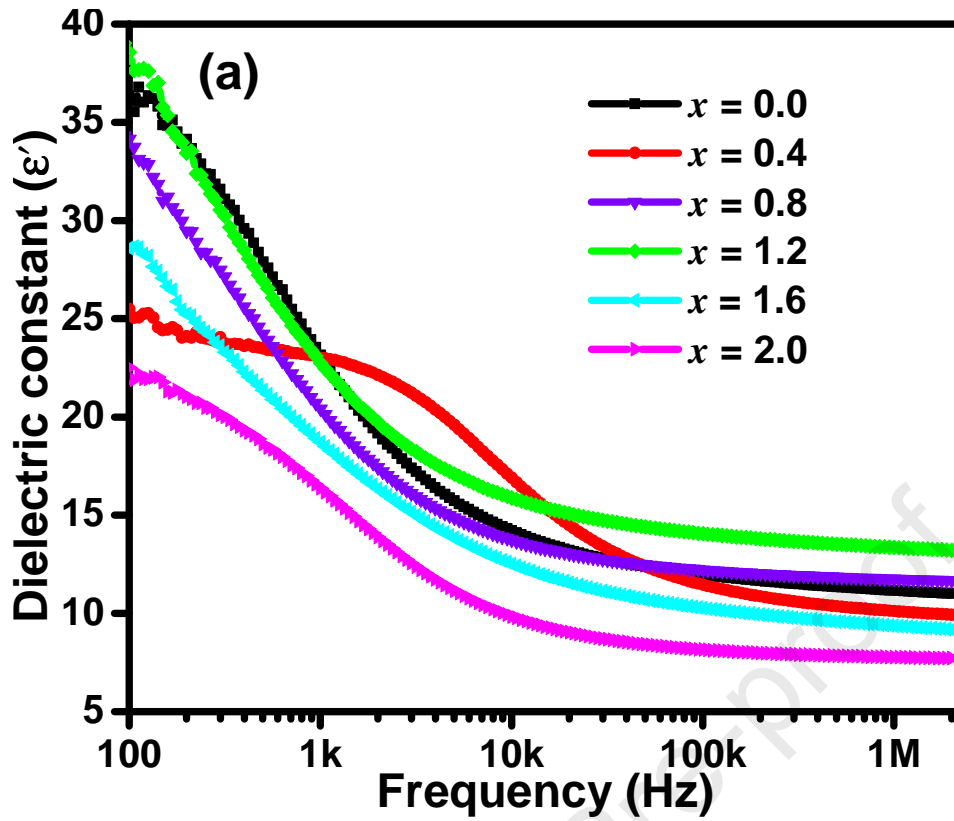


Fig.8. Variation in Mössbauer parameters (a) isomer shift, (b) quadrupole splitting, (c) hyperfine magnetic field, (d) average isomer shift, (e) average hyperfine field, (f) average quadrupole splitting, (g) relative area of Fe^{3+} and Fe^{2+} (%) and (h) relative area of sextets and saturation magnetization (M_s) with Ga-substitution (x).



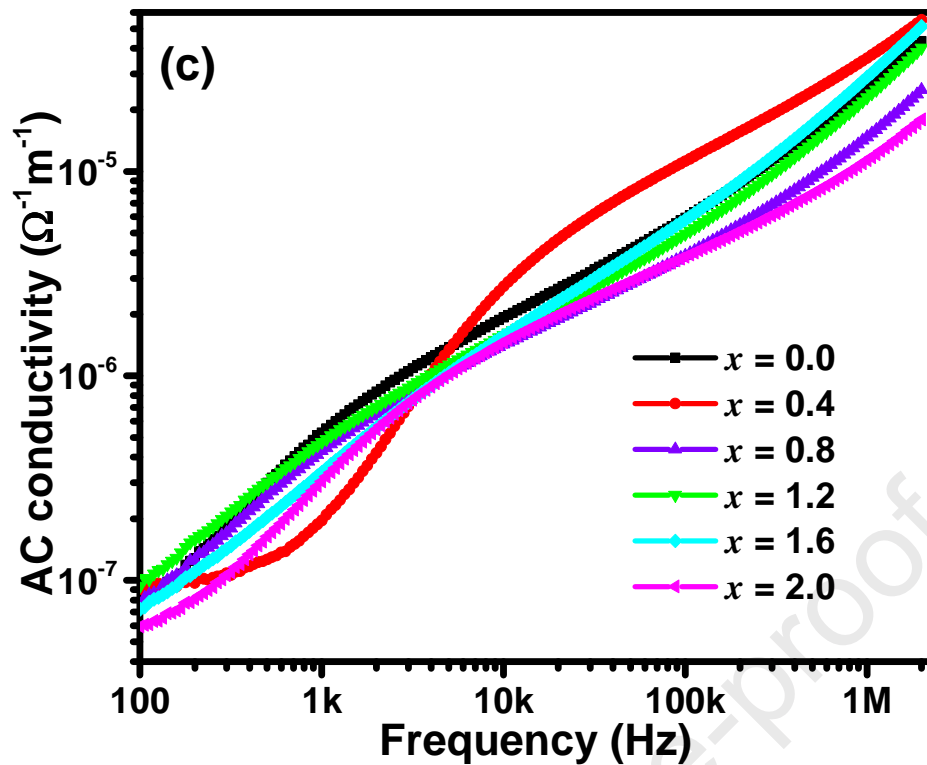
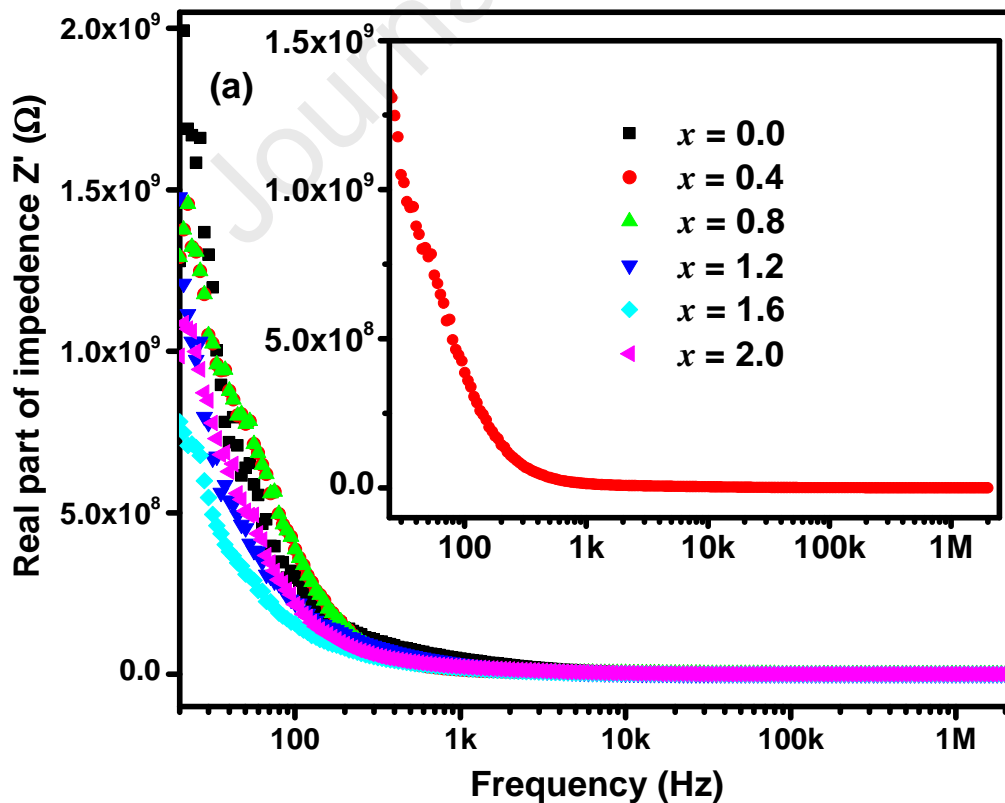


Fig. 9. Variation of (a) real dielectric constant (ϵ'), (b) dielectric loss tangent ($\tan \delta$) and (c) AC conductivity (σ_{ac}) as a function of frequency for $\text{Sr}_3\text{Ga}_x\text{Co}_{2-x}\text{Fe}_{24}\text{O}_{41}$ ($x = 0.0, 0.4, 0.8, 1.2, 1.6,$ and 2.0) hexaferrite powder samples



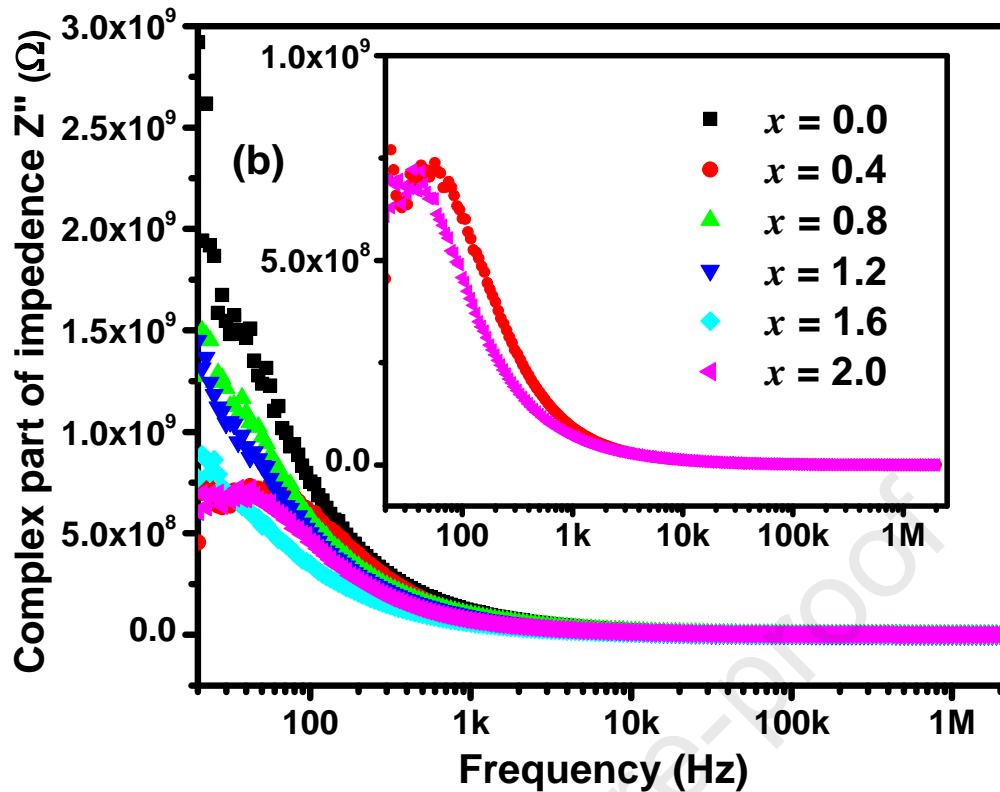
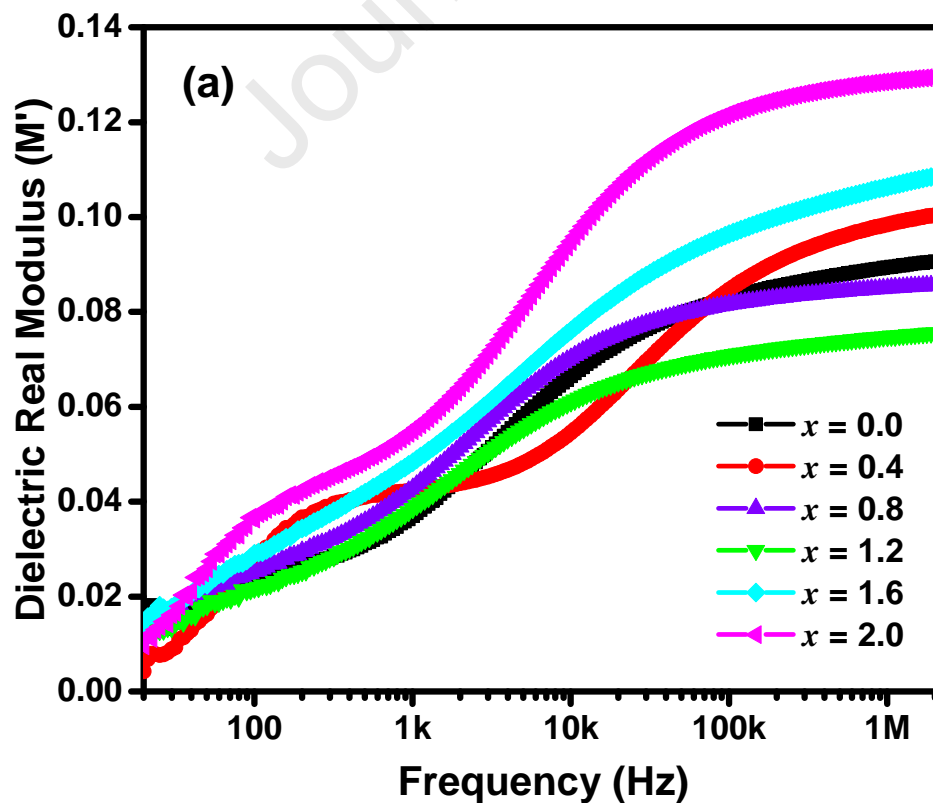


Fig.10. Variation of (a) real dielectric impedance (Z' (ohm)) with frequency for $\text{Sr}_3\text{Ga}_x\text{Co}_{2-x}\text{Fe}_{24}\text{O}_{41}$ ($x = 0.0, 0.4, 0.8, 1.2, 1.6,$ and 2.0) hexaferrite samples and its inset shows a clear view of sample $x = 0.4$, (b) complex dielectric impedance (Z'' (ohm)) of all samples and its inset shows the expanded view of samples $x = 0.4$ and 2.0 heated at 1150°C for 5 h



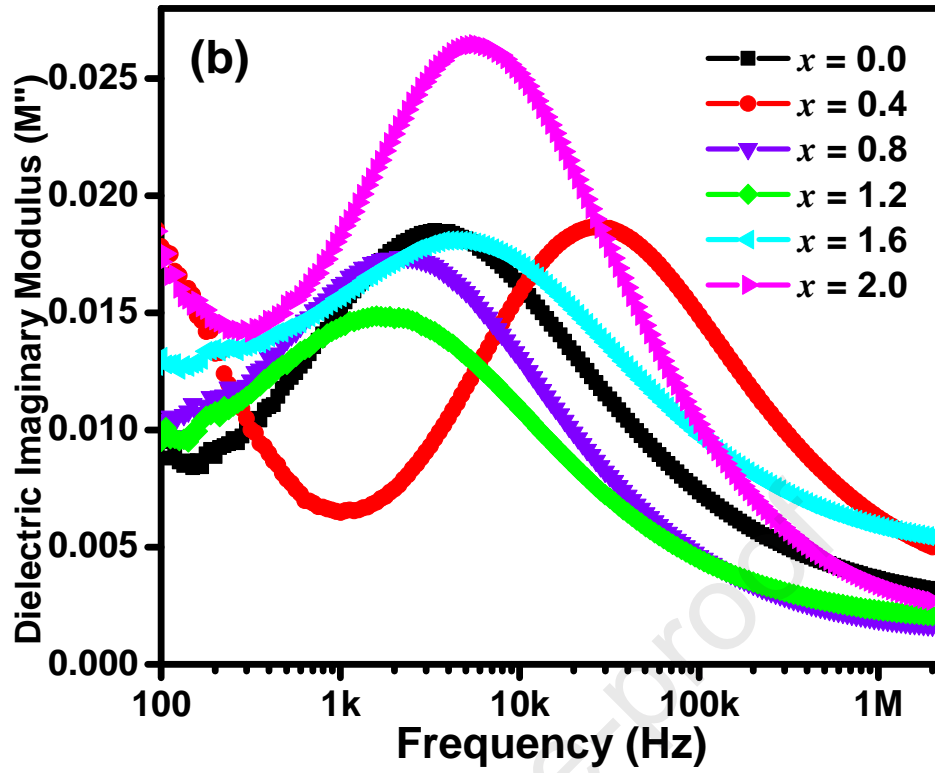


Fig. 11 (a). Real part of dielectric modulus (M') and (b) Imaginary part of dielectric modulus (M'') as a function of frequency for $\text{Sr}_3\text{Ga}_x\text{Co}_{2-x}\text{Fe}_{24}\text{O}_{41}$ ($x = 0.0, 0.4, 0.8, 1.2, 1.6, \text{ and } 2.0$) hexaferrite samples heated at 1150°C for 5 h

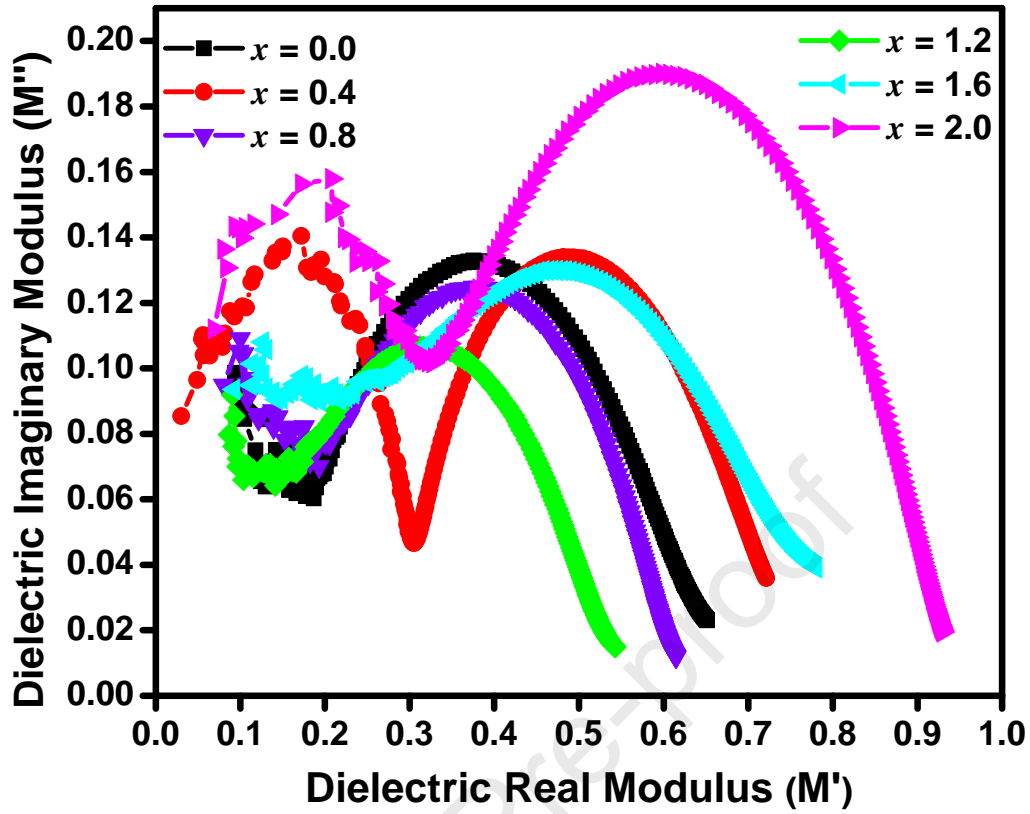
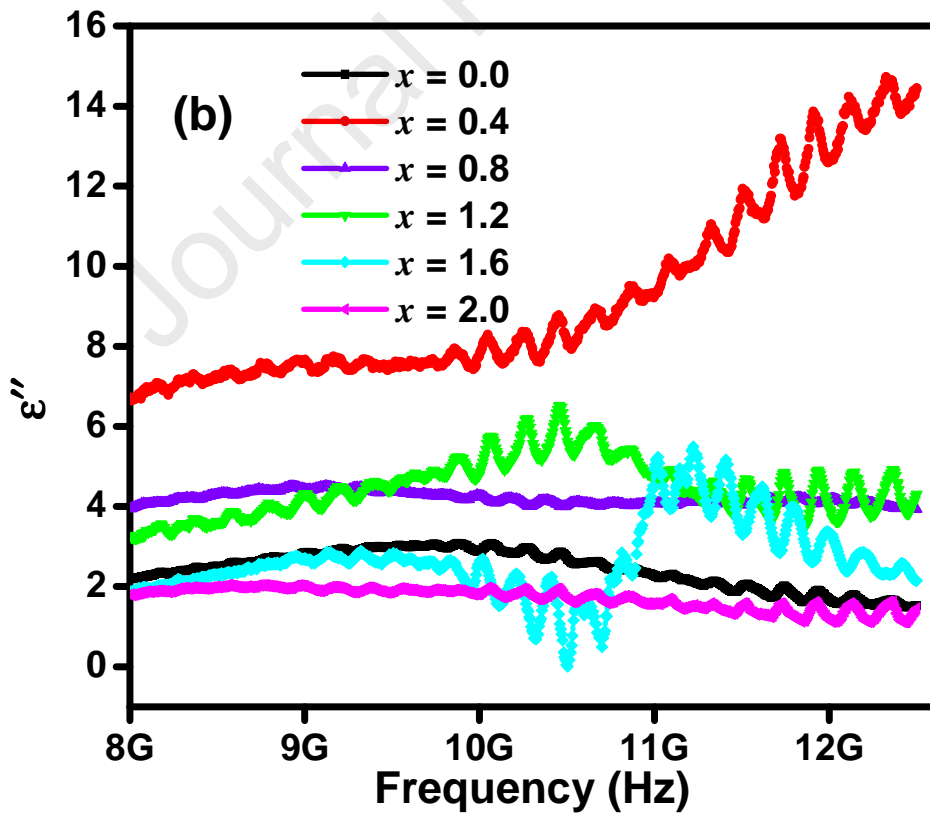
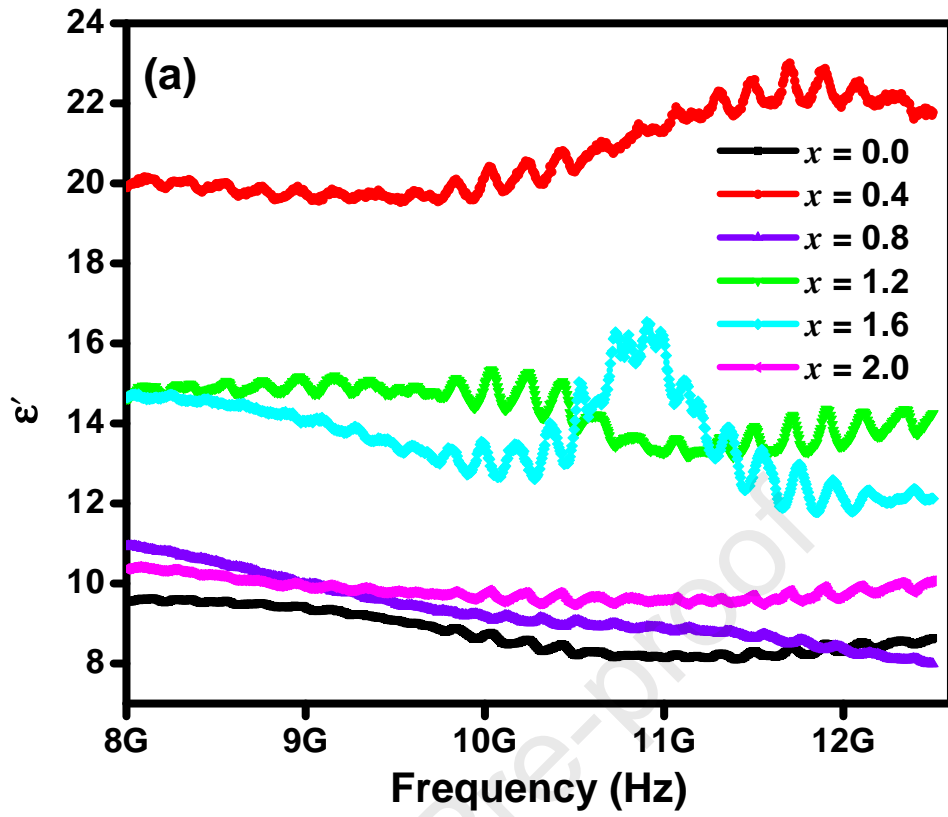


Fig. 12. Cole-Cole plot of $Sr_3Ga_xCo_{2-x}Fe_{24}O_{41}$ ($x = 0.0, 0.4, 0.8, 1.2, 1.6,$ and 2.0) hexaferrite samples heated at $1150\text{ }^\circ\text{C}$ for 5 h.



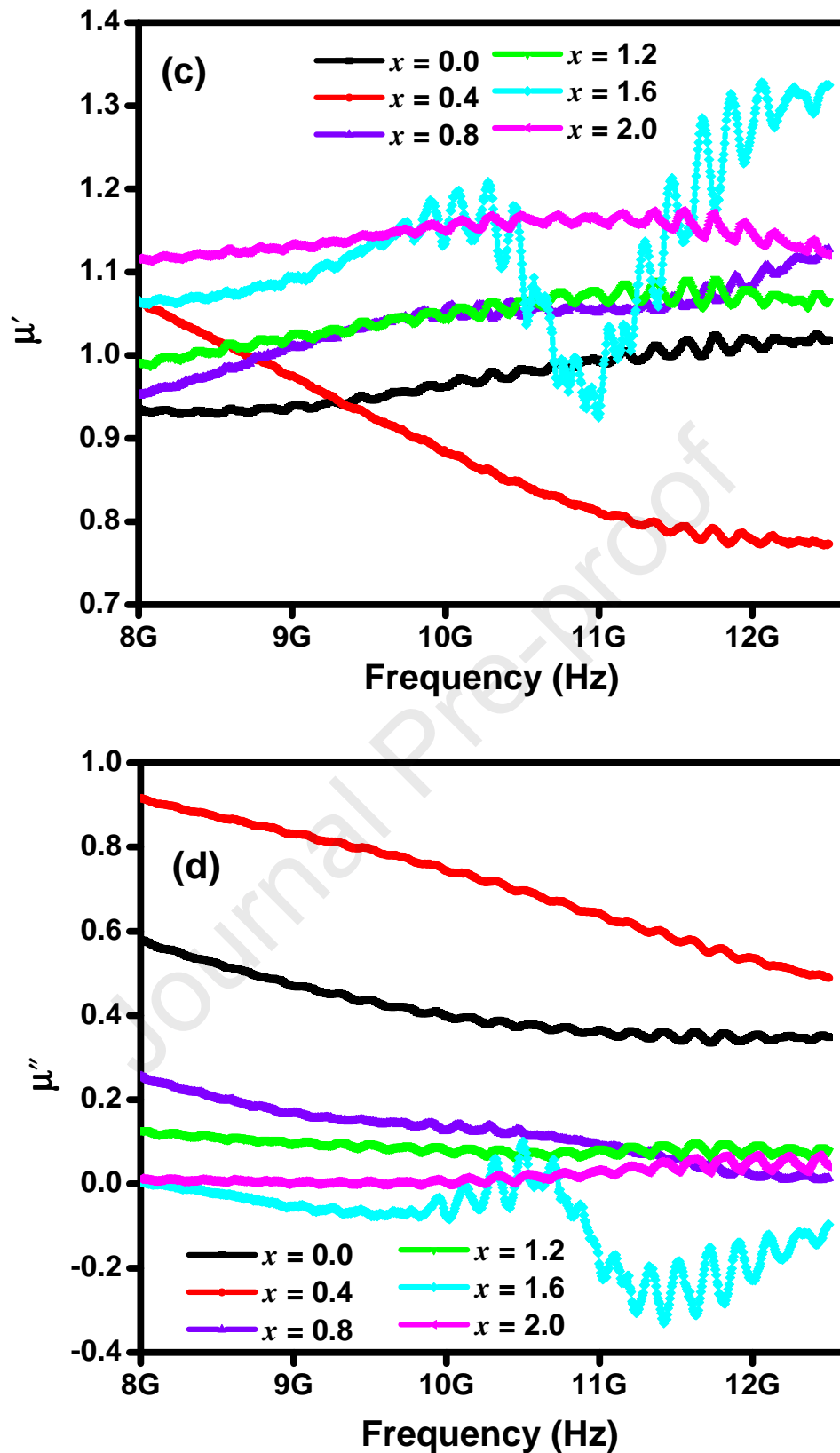
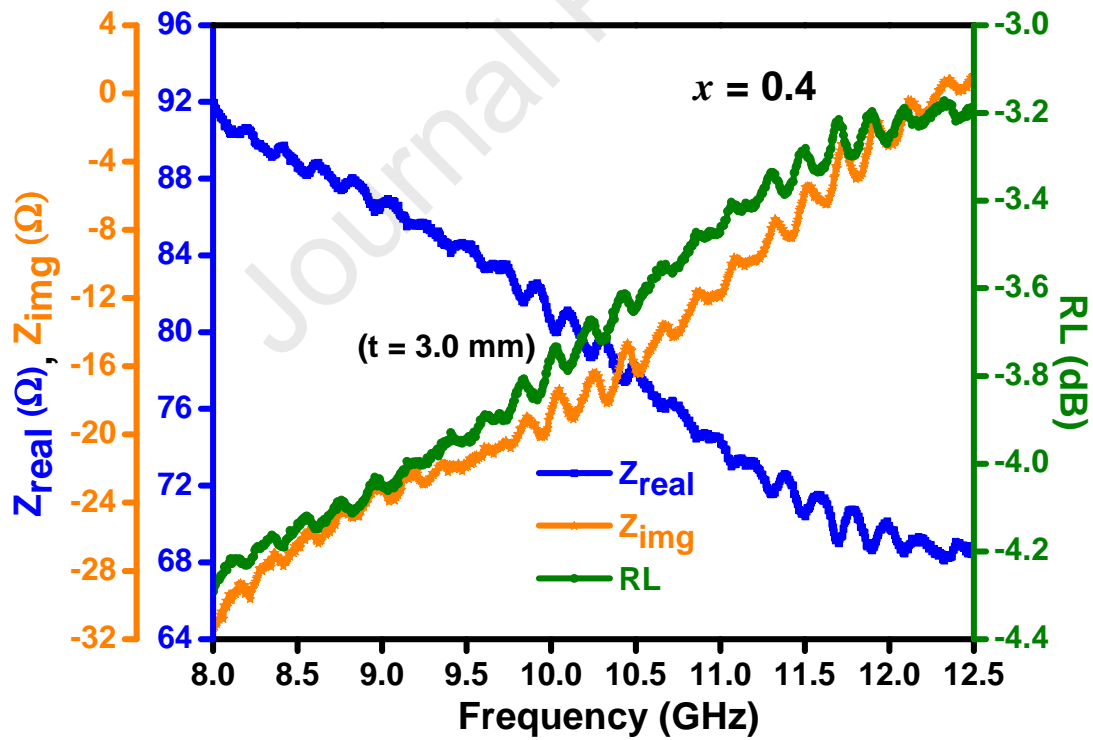
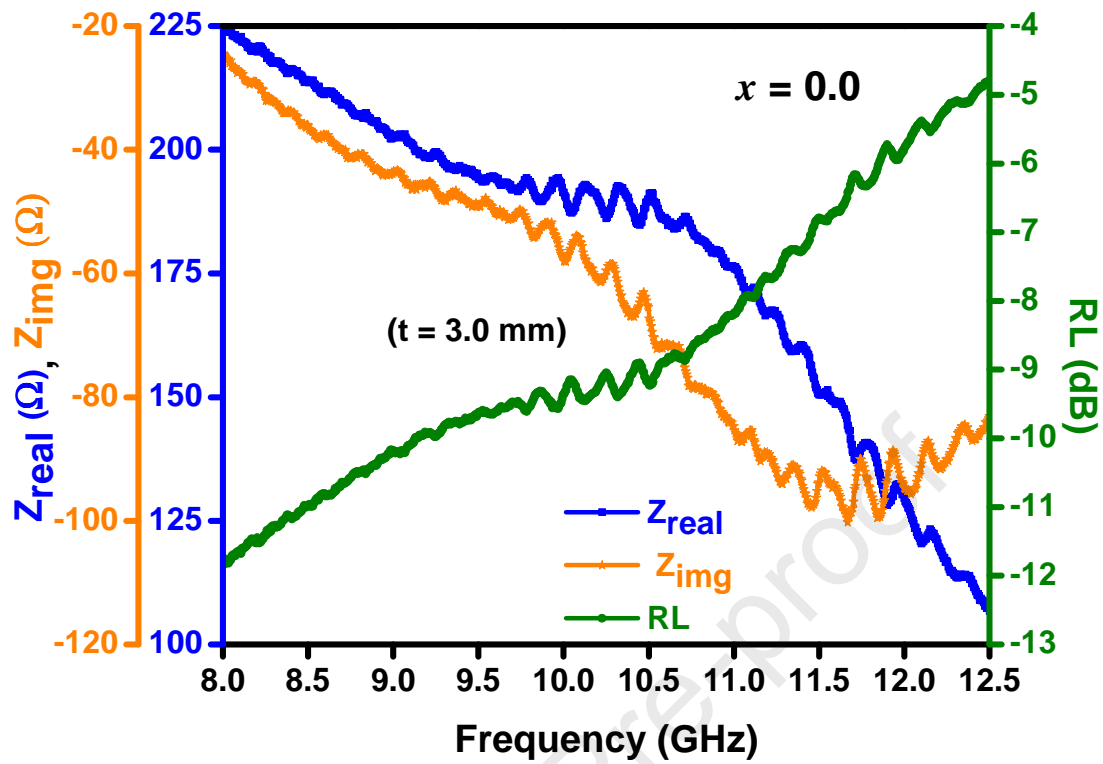


Fig. 13. Variation of (a) real dielectric constant (ϵ'), (b) dielectric loss (ϵ''), (c) real permeability μ' and (d) magnetic loss (μ'') with the frequency between 8 GHz-13 GHz



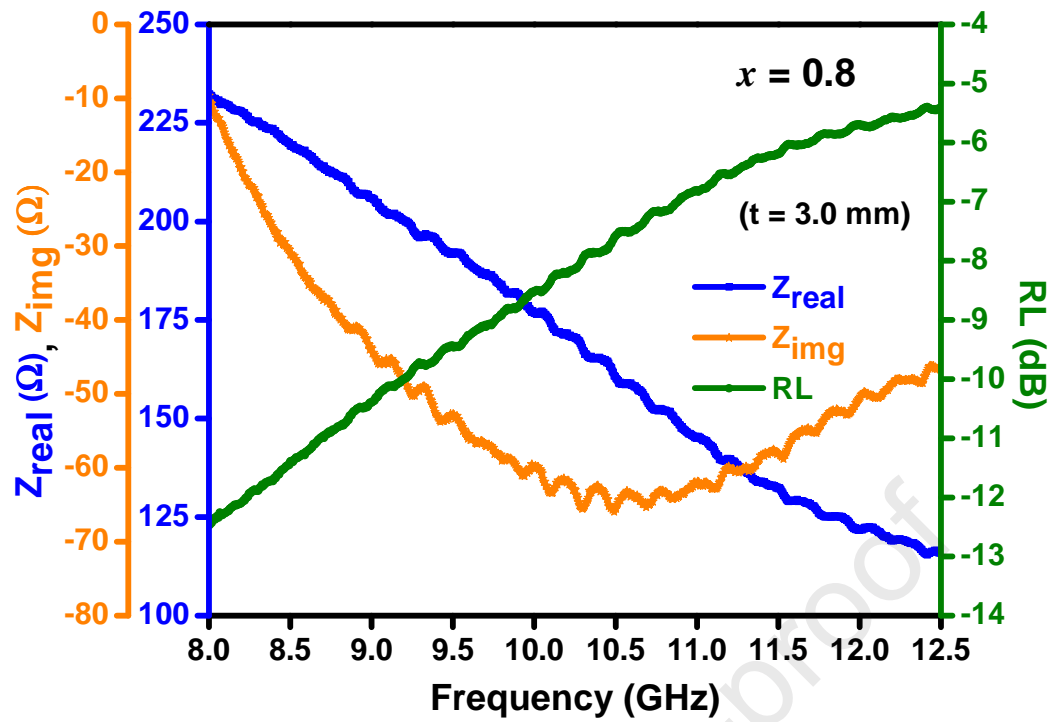


Fig.14. Variation of reflection loss (RL) peak, real impedance (Z_{real}) and imaginary impedance (Z_{img}) as a function of frequency for samples $x = 0.0, 0.4,$ and 0.8 at 3.0 mm thickness

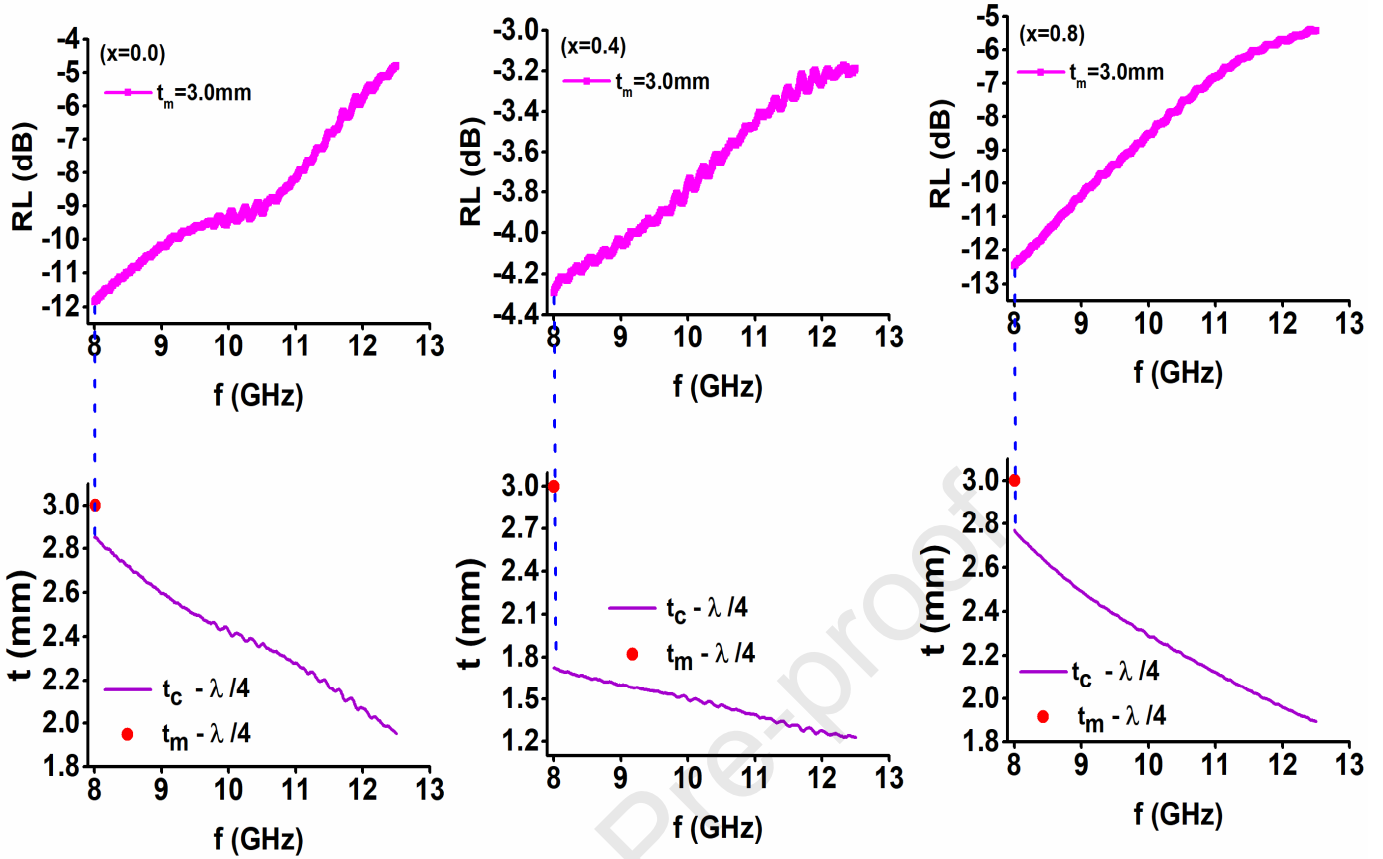


Fig. 15. Quarter Wavelength Mechanism in samples $x = 0.0, 0.4$ and 0.8

List of tables

Table 1. Lattice parameters, c/a ratio, FWHM, unit cell volume and average crystallite size of $\text{Sr}_3\text{Co}_{2-x}\text{Ga}_x\text{Fe}_{24}\text{O}_{41}$ ($x = 0.0, 0.4, 0.8, 1.2, 1.6,$ and 2.0) hexaferrite powder samples, heated at 1150°C for 5 h.

Ga content (x)	Lattice parameters		c/a ratio	FWHM ($^\circ$)	Unit cell volume $V(\text{\AA}^3)$	Average crystallite size $D_{xrd}(\text{nm})$
	$a(\text{\AA})$	$c(\text{\AA})$				
0.0	5.921	52.493	8.8656	0.3832	1593.71	22.56
0.4	5.919	52.483	8.8669	0.3538	1592.33	24.60
0.8	5.913	52.472	8.8740	0.3776	1588.77	22.89
1.2	5.909	52.462	8.8783	0.2950	1586.32	29.30

1.6	5.907	52.456	8.8803	0.2888	1585.06	30.08
2.0	5.905	52.441	8.8808	0.3644	1583.54	23.83

Table 2. The X-ray density, bulk density and porosity of $\text{Sr}_3\text{Co}_{2-x}\text{Ga}_x\text{Fe}_{24}\text{O}_{41}$ ($x = 0.0, 0.4, 0.8, 1.2, 1.6, 2.0$) hexaferrite powder samples heated at 1150 °C for 5 h.

Ga content (x)	X-ray density	Bulk density	Porosity
	d_x (g/cm^3)	d_B (g/cm^3)	P (%)
0.0	4.95	3.83	16.70
0.4	4.96	3.80	23.49
0.8	4.99	3.41	31.56
1.2	5.00	3.59	28.08
1.6	5.01	3.63	27.59
2.0	5.03	3.49	30.67

Table 3. Magnetic parameters for $\text{Sr}_3\text{Co}_{2-x}\text{Ga}_x\text{Fe}_{24}\text{O}_{41}$ ($x = 0.0, 0.4, 0.8, 1.2, 1.6, \text{ and } 2.0$) hexaferrites

Ga content (x)	Saturation Magnetisation	Remanant Magnetisation	M_r/M_s	Coercivity	Coercivity	Anisotropy field
	M_S ($\text{A m}^2\text{kg}^{-1}$)	M_r ($\text{A m}^2\text{kg}^{-1}$)		H_C (kA m^{-1})	H_C (Oe)	H_a (kA m^{-1})
0.0	80.27	0.10	0.001	0.14	1.79	1237.47
0.4	97.94	0.37	0.003	0.46	5.74	917.56
0.8	75.56	3.55	0.046	3.99	50.0	1147.19
1.2	88.74	12.27	0.138	18.47	231.6	1353.96
1.6	69.99	24.76	0.353	94.53	1185.0	1750.44

2.0	84.01	36.38	0.432	186.87	2342.55	1807.13
------------	-------	-------	-------	--------	---------	---------

Table 4. The values of hyperfine field (H_{hf}), isomer shift (δ), quadrupole splitting (Δ), line width (Γ) and relative area (R_A) of tetrahedral (tetra), octahedral (octa) and trigonal bipyramidal (tbp) sites of Fe^{3+} ions for Ga-substituted $Sr_3Co_{2-x}Ga_xFe_{24}O_{41}$ ($x = 0.0, 0.4, 0.8, 1.2, 1.6,$ and 2.0) hexaferrites, derived from Mössbauer spectra recorded at room temperature.

*Isomer shift values are with respect to α -Fe metal foil

Ga-content (x)	Iron sites	Ionic state (high spin)	Relative area (R_A) (%)	Isomer shift* (δ) mm/s ± 0.01	Quadrupole splitting (Δ) mm/s ± 0.02	Hyperfine field (H_{hf}) Tesla ± 0.1	Outer line width (Γ) mm/s ± 0.05	Fitting quality (χ^2)
0.0	Sextet-A	Fe^{3+}	9.43	0.368	-0.08	51.97	0.343	
	Sextet-B	Fe^{3+}	16.88	0.435	0.039	49.475	0.565	
	Sextet-C	Fe^{3+}	16.98	0.204	-0.083	48.91	0.481	
	Sextet-D	Fe^{3+}	9.42	0.389	-0.075	45.74	0.648	1.57
	Sextet-E	Fe^{3+}	6.67	0.266	-0.797	41.227	0.749	
	Sextet-F	Fe^{3+}	39.68	0.357	-0.174	39.464	0.663	
	Doublet-A	Fe^{3+}	0.94	0.228	0.521	--	0.547	
0.4	Sextet-A	Fe^{3+}	10.69	0.391	-0.079	52.215	0.301	
	Sextet-B	Fe^{3+}	8.69	0.476	0.049	50.017	0.274	
	Sextet-C	Fe^{3+}	22.66	0.219	-0.084	49.299	0.492	
	Sextet-D	Fe^{3+}	4.65	0.467	0.242	47.435	0.589	1.84
	Sextet-E	Fe^{3+}	15.17	0.394	-0.357	40.045	0.478	
	Sextet-F	Fe^{3+}	23.10	0.377	-0.094	39.483	0.312	
	Doublet-A	Fe^{3+}	1.09	0.231	0.571	--	0.389	

	Sextet-G	Fe ³⁺	13.95	0.166	-0.659	41.074	1.832	
0.8	Sextet-A	Fe ³⁺	5.04	0.401	-0.033	51.996	0.287	
	Sextet-B	Fe ³⁺	19.58	0.451	0.105	49.522	0.545	
	Sextet-C	Fe ³⁺	17.65	0.185	-0.036	48.924	0.443	
	Sextet-D	Fe ³⁺	9.99	0.431	-0.059	45.311	0.895	
	Doublet-B	Fe ²⁺	0.27	1.887	4.228	--	0.23	
	Sextet-E	Fe ³⁺	25.99	0.359	-0.149	39.785	0.5967	1.40
	Doublet-A	Fe ³⁺	0.86	0.33	0.443	--	0.565	
	Sextet-F	Fe ³⁺	13.01	0.354	0.408	40.95	0.455	
	Sextet-G	Fe ³⁺	7.47	0.435	0.161	36.284	0.674	
	Doublet-C	Fe ²⁺	0.14	0.601	4.78	--	0.23	
1.2	Sextet-A	Fe ³⁺	9.17	0.449	0.271	50.613	0.396	
	Sextet-B	Fe ³⁺	21.75	0.409	0.141	48.69	0.591	
	Sextet-C	Fe ³⁺	13.19	0.134	-0.066	48.812	0.385	
	Sextet-D	Fe ³⁺	5.56	0.462	-0.036	44.612	0.5	
	Doublet-B	Fe ²⁺	0.21	1.518	2.764	--	0.23	
	Sextet-E	Fe ³⁺	9.32	0.384	-0.054	39.159	0.472	1.46
	Doublet-A	Fe ³⁺	0.63	0.136	0.489	--	0.516	
	Sextet-F	Fe ³⁺	28.65	0.352	0.383	41.154	0.456	
	Sextet-G	Fe ³⁺	11.19	0.392	0.341	35.964	0.571	
	Doublet-C	Fe ²⁺	0.33	0.605	4.81	--	0.23	
1.6	Sextet-A	Fe ³⁺	10.04	0.295	0.267	51.284	0.257	
	Sextet-B	Fe ³⁺	12.49	0.371	0.21	48.939	0.564	
	Sextet-C	Fe ³⁺	21.43	0.14	0.117	48.536	0.454	
	Sextet-D	Fe ³⁺	1.94	0.73	-0.049	44.214	0.199	
	Doublet-B	Fe ²⁺	0.71	1.512	2.803	--	0.319	
	Sextet-F	Fe ³⁺	26.46	0.287	0.399	40.907	0.369	

	Doublet-A	Fe ³⁺	0.65	0.219	0.882	--	0.851	
	Sextet-E	Fe ³⁺	7.81	0.288	0.469	41.949	0.506	
	Sextet-G	Fe ³⁺	17.91	0.325	0.423	36.15	0.702	
	Doublet-C	Fe ²⁺	0.55	0.393	4.729	--	0.407	
	Sextet-A	Fe ³⁺	12.10	0.348	0.28	51.364	0.263	
	Sextet-B	Fe ³⁺	11.26	0.423	0.193	49.177	0.482	
	Sextet-C	Fe ³⁺	19.73	0.203	0.125	48.694	0.397	
	Sextet-D	Fe ³⁺	1.39	0.203	0.626	46.057	0.16	
2.0	Doublet-B	Fe ²⁺	0.62	1.4	2.92	--	0.327	
	Sextet-E	Fe ³⁺	4.37	0.575	1.148	39.325	0.448	1.61
	Doublet-A	Fe ³⁺	0.29	0.265	0.13	--	0.23	
	Sextet-F	Fe ³⁺	35.26	0.335	0.399	41.095	0.379	
	Sextet-G	Fe ³⁺	14.49	0.356	0.439	36.02	0.553	
	Doublet-C	Fe ²⁺	0.49	0.498	4.924	--	0.23	

Declaration of interests

The authors declare that they have no known competing financial interests or personal relationships that could have appeared to influence the work reported in this paper.

Preksha N. Dhruv, Robert C. Pullar, Charanjeet Singh, Francisco E. Carvalho, Rajshree B. Jotania, Sher Singh Meena, Jasbir Singh